

A Novel Methodology for Cancer Diagnosis and Treatment Using New Generation Microfluidic Devices: Hydrodynamic Cavitation on a Chip

By
İlayda Namlı

Submitted to the Graduate School of Natural Science and Engineering In partial fulfillment of the requirement for the degree of Master of Science in Material Science and Nano Engineering

Sabanci University

July 2022

© İlayda Namlı 2022
All Rights Reserved

ABSTRACT

A Novel Methodology for Cancer Diagnosis and Treatment Using New Generation Microfluidic Devices: Hydrodynamic Cavitation on a Chip

İlayda Namlı

MSc. Thesis, July 2022

Advisor: Prof. Ali Koşar

Co-Advisor: Dr. Sibel Çetinel

Keywords: Circulating Tumor Cells, Hydrodynamic Cavitation, Circulating Tumor Cell Detection, Cavitation on a Chip, Cancer Treatment

Hydrodynamic cavitation (HC) is a phase change phenomenon, where energy release in a fluid occurs upon the collapse of bubbles, which form due to the low local pressures. Although macro-scale hydrodynamic cavitation has a very destructive effect due to the high released energy from the cavitation bubble explosion, damaging effects of cavitation could be minimized and utilized for biomedical applications through micro-scale hydrodynamic cavitation inside a miniaturized microfluidic device. Since microfluidic devices enable the performance of controlled experiments by enabling spatial control over the cavitation process and by precisely monitoring its evolution. Early cancer diagnosis and effective therapeutic technologies appears to be inevitable needs for the human health. In this regard, this thesis presents comprehensive investigation and analysis related to role of the HC on circulating tumor cell (CTC) detection and cancer treatment through *in vitro* studies by utilizing cell culture and human blood samples. Performed *in vitro* experiments demonstrate that micro-scale HC, which is an emerging tool in biological applications, is a promising approach to investigate different cellular responses and to increase the chemotherapeutic efficacy of the anticancer drug and to rapidly detect CTCs.

ÖZET

Yeni Nesil Mikroakışkan Cihazları Kullanarak Kansere Teşhisi ve Tedavisinde Yeni Bir Metodoloji: Çip Üstü Hidrodinamik Kaviteasyon

İlayda Namlı

Yüksek Lisans Tezi, Temmuz 2022

Danışman: Prof. Ali KOŞAR

Yardımcı Danışman: Dr. Sibel Çetinel

Anahtar Kelimeler: Dolaşan Tümör Hücreleri, Hidrodinamik Kaviteasyon, Dolaşan Tümör Hücrelerinin Tespiti, Çip Üzerinde Kaviteasyon, Kansere Tedavisi

Hidrodinamik kaviteasyon (HC), düşük yerel basınçlar nedeniyle oluşan kabarcıkların çökmesi vasıtasıyla bir sıvıda enerji salınımının meydana geldiği bir faz değişimi fenomenidir. Makro ölçekli hidrodinamik kaviteasyon, kaviteasyon kabarcığı patlamasından dolayı salınan yüksek enerji nedeniyle çok yıkıcı bir etkiye sahip olsa da, minyatürleştirilmiş bir mikroakışkan cihaz içinde mikro ölçekli hidrodinamik kaviteasyon yoluyla kaviteasyonun zararlı etkileri en aza indirilebilir ve biyomedikal uygulamalar için kullanılabilir. Mikroakışkan cihazlar, kaviteasyon süreci üzerinde uzamsal kontrol sağlayarak ve gelişimini hassas bir şekilde izleyerek kontrollü deneylerin performansını mümkün kılar. Erken kansere teşhisi ve etkili tedavi teknolojileri insan sağlığı için kaçınılmaz ihtiyaçlar olarak görünmektedir. Bu bağlamda, bu tez, hücre kültürü ve insan kan örneklerini kullanarak *in vitro* çalışmalar yoluyla HC'nin dolaşımdaki tümör hücresi (CTC) tespiti ve kansere tedavisi üzerindeki rolü ile ilgili kapsamlı araştırma ve analiz sunmaktadır. Gerçekleştirilen *in vitro* deneyler, biyolojik uygulamalarda ortaya çıkan bir araç olan mikro ölçekli HC'nin, farklı hücresel tepkileri araştırmak ve antikanser ilacının kemoterapötik etkinliğini artırmak ve CTC'leri hızlı bir şekilde saptamak için umut verici bir yaklaşım olduğunu

göstermektedir.

ACKNOWLEDGMENTS

I would like to express my most profound appreciation to Prof. Ali Koşar, Dr. Sibel Çetinel, and Dr. Morteza Ghorbani for their continuous support and guidance throughout my thesis. Their vast knowledge and broad experience have encouraged me throughout my academic research.

I would like to thank esteemed Dr. Ozlem Kutlu and Dr. Huseyin Uvet for agreeing to read the manuscript and to participate in this thesis defense.

I would like to thank my groupmates and collaborators, especially Seyedali Seyedmirzaei Sarraf and Zeynep Karavelioğlu for their contributions and supports during my thesis.

Last but not least, I am grateful to have such a family who encouraged and supported me throughout my academic life.

Table of Contents

1. CHAPTER ONE: INTRODUCTION	1
1.1. Cancer Diagnosis and Treatment	1
1.1.1. Cavitation	3
1.1.2. Micro-scale Cavitation	5
1.1.3. Micro-scale Cavitation in biomedical engineering	5
1.1.3.1. Cell Lysis, Deformation and DNA extraction	5
1.1.3.2. Cell Membrane Permeabilization, Drug delivery	7
1.1.3.3. Blood-Brain-Barrier	9
1.1.3.4. Cell Sorting/Focusing	10
1.2. Motivation and Novel Aspects	11
1.3. Thesis Objectives	12
2. CHAPTER TWO: HYDRODYNAMIC CAVITATION ON A CHIP AS A CANCER DIAGNOSTIC (CIRCULATING TUMOR CELL DETECTION) TOOL	13
2.1. Research Objectives	13
2.2. Experimental Method	13
2.2.1. Cell Culture Sample Preparation	13
2.2.2. Blood Sample Preparation.	15
2.2.3. Microfluidic Device Design, Fabrication and Experimental Procedure	16
2.2.3.1. Fabrication Method and Device Configuration	16
2.2.3.2. Experimental Setup of Microfluidic System (HCOC)	18
2.2.4. The HC-On-Chip (HCOC) Experiments and CTC Detection Protocols:	19
2.2.4.1. Cavitation Inception Measurement Procedure of Different Working Fluids	19
2.2.4.2. Cavitation Inception of Medium with Different Number of CTCs	20
2.2.5. Characterization methods. Scanning Electron Microscopy (SEM)	21
2.2.6. Cell Staining	21
2.2.7. Statistical Analysis	22
2.3. Results	22

2.3.1.	Cavitation Inception	22
2.3.2.	Relationship between Cavitation Inception and Concentration of Cell-CTC Enrichment	25
2.3.3.	Cavitation Inception of Blood Sample	26
2.4.	Discussions	27
3.	CHAPTER THREE: CANCER TREATMENT USING FACILE HYDRODYNAMIC ON A CASCADE DEVICE	32
3.1.	Research Objectives	32
3.2.	Experimental Method	32
3.2.1.	Cell Culture	32
3.2.2.	Hydrodynamic Cavitation Treatment	33
3.2.3.	Microfluidic Device Design, Fabrication and Experimental Procedure	33
3.2.3.1.	Fabrication Method and Device Configuration	33
3.2.4.	Determination of Cell Proliferation Under DOX Treatment and Hydrodynamic Cavitation	34
3.2.5.	Morphological Analysis of Cells Upon Hydrodynamic Cavitation	34
3.2.6.	Calcein AM/PI Staining for Live/Dead Cell Imaging	35
3.2.7.	Detection of Enhanced Cell Permeability by CDs	35
3.2.8.	Production of PZT Transducer-Embedded Microfluidic Chambers	36
3.2.9.	Optic Measurement of Cell Stiffness by Acousto-Holographic	36
3.2.10.	Statistical Analysis	36
3.3.	Results	37
3.3.1.	Characterization of the Zones of Cellular Response	38
3.3.2.	Characterization of The Morphological Changes After HC Exposure	39
3.3.3.	Fluorescent Examination of Live/Dead Cells by Calcein AM/PI Staining	40
3.3.4.	Demonstration of Cellular Uptake Upon HC Exposure	41
3.3.5.	Changes in Cell Viability After HC + DOX Treatment	43
3.3.6.	Effect of The HC on Biomechanical Properties of The Cells	46
3.4.	Discussions	47

4. CONCLUSIONS AND FUTURE RESEARCH DIRECTIONS	52
5. REFERENCES	54

List of Tables

Table 1: The geometrical properties of the microfluidic device without roughness (Chip-wo-R). 17

Table 2: The geometrical properties of the microfluidic device with roughness (Chip-R). 18

List of Figures

Figure 1: **A)** Schematic of cell culture preparation before the experiments and **B)** blood sample preparation before cavitation tests. A.1) The group including only RPMI 1640 cell culture medium, A.3-4) adding Jurkat cells on a flask, A.5) seeding MDA-MB-231 cells, cultured in DMEM previously, on a flask. B.1) Blood samples were collected from volunteers into sample tubes. B.2) Red blood cells were lysed, centrifuged and discarded. B.3) Remaining samples divided into two groups considering cell concentration and CTCs were spiked into one of the groups. B.4) Each sample were introduced to different microfluidic devices with exactly same configuration. B.5) Cavitation inception pressures were recorded for each group and graphs were plotted. 15

Figure 2: **a)** Photoresist casting on a silicon dioxide-coated wafer. **b)** Lithography with photoresist coating for channel design. **c)** SiO₂ etching, **d)** photoresist removal, **e)** Lithography for the inlet–outlet and pressure ports. **f)** DRIE for Si to open inlet-outlet and pressure ports. **g)** Resist stripping and Ti, Al coating also DRIE for etching through the wafer **h)** Wet etching of Al and Ti. **i)** Wet etching of SiO₂. **j)** Anodic bonding of the silicon wafer to glass. 16

Figure 3: Experimental setup and microfluidic chip details. The cavitation inception is detected using the high-speed camera and the pertinent pressure to the instance of cavitation inception is recorded as the cavitation inception pressure. 20

Figure 4: Sample fixation protocol for SEM analysis 21

Figure 5: **A)** The graph shows that cavitation inception pressures of different working fluids through microfluidic device without roughness (Chip-wo-R). The working fluids are RPMI 1640 cell culture medium, Jurkat, CTC and Jurkat+CTC. Error bars indicate standard deviation. **B)** Probability distribution graph of Medium, Medium with Jurkat Cells and Medium with Jurkat Cells+CTCs in terms of cavitation inception pressure. The inception pressure data was derived 8 times for each sample and the nonlinear fit was performed in MATLAB to show the inception pressure for each sample as a Gaussian distribution. 23

Figure 6: The graph shows that cavitation inception pressures of different working fluids through microfluidic device with roughness (Chip-R). The working fluids are RPMI 1640 cell culture medium, Jurkat, CTC and Jurkat+CTC. Error bars indicate standard deviation. 24

Figure 7: Column graph of the cavitation inception pressure of Jurkat, 300 CTCs/mL

+Jurkat, 100 CTCs/mL +Jurkat cells and 50 CTCs/mL+Jurkat cells	25
Figure 8: SEM images of (a) MDA-MB-231 cell line (b) Jurkat cell line. Fluorescence microscopy images of the cells after staining Jurkat Cell (c), MDA-MB-231 (d) and size distribution of the Jurkat and MDA-MB-231 cells (e).	26
Figure 9: Column graph of the cavitation inception pressure of different blood samples.	27
Figure 10: Schematic summary of experimental procedures before and after hydrodynamic cavitation exposure.	34
Figure 11: Illustration of zones of cellular effect created by HC.	37
Figure 12: Microfluidic device configuration. Inlet Region Length (L_1) is 2000 μm , Micro-orifice Length (L_2) is 1000 μm , Outlet Region Length (L_3) is 2000 μm , Outlet Region Width (W_1) is 7800 μm , Micro-orifice Width (W_2) is 300 μm .	38
Figure 13: A) Phase-contrast image of Beas-2B cells upon HC exposure. HC exposure results in detachment of the cells from the exposure area. The cells adjacent to the exposure region are still attached to the surface. The yellow line separates the different regions based on cellular response. B) zoom-in image of the region of attached cells and C) zoom- in image of the detached cells from the surface.	39
Figure 14: Detailed morphological SEM images of the lysed A) A549 cell, B) SHSY-5Y cell, C) Beas-2B cell D) HUVEC cell in the HC exposure area (lysis region). Cavitation bubbles damage the cell membrane due to imposing upon direct HC exposure, and different sizes of the pores are shown in the images indicated by red circles.	40
Figure 15: Fluorescent images of the A) A549 cells and B) Beas-2B cells after Calcein AM-PI staining following HC exposure. The different regions appear based on cell attachment upon HC exposure. Most of the detached cells are washed with the help of HC. Some cells keep their attachment, but not their viability. The green color represents the viable cells, while the red color refers to dead cells.	41
Figure 16: A) The combined fluorescent and bright-field images of the Beas-2B cells. B) Green color indicates the CDs uptaken by the cells closer to the HC application region. C) The image shows that the cells could not achieve cellular uptake due to the large distance from the HC application area.	42
Figure 17: The combined fluorescent and bright-field images of the Beas-2B cells introduced CDs at different time periods. The cells introduced to CDs for A) 10 min, B)	

30 min, **C**) 1 h and **D**) 3 h without HC exposure. Green color indicates CDs uptaken by the cells. 43

Figure 18: Cell viability profiles of Beas-2B and A549 cells. Cell viability is shown for cases without any treatment and exposure (control), with treatment different concentrations of DOX. [**A**) 05 mM, **B**) 1 mM, **C**) 2 mM], upon HC exposure and after different concentration of DOX combination with HC exposure. 44

Figure 19: Cell viability profiles of HUVEC, SH-SY5Y, Beas-2B and A549 cells. Cell viability is shown for cases without any treatment and exposure (control), with treatment different concentrations of DOX. [**A**) 05 mM, **B**) 1 mM, **C**) 2 mM], upon HC exposure and after different concentration of DOX [**A**) 05 mM, **B**) 1 mM, **C**) 2 mM] combination with HC exposure. 45

Figure 20: Acousto-holographic stiffness distribution of **(a)** A549 control cells, **(b)** BEAS-2B control cells, **(c)** HC-exposed A549 cells, and **(d)** HC-exposed BEAS-2B cells. 47

1. CHAPTER ONE: INTRODUCTION

1.1.Cancer Diagnosis and Treatment

Despite contemporary advances in healthcare technologies, cancer globally remains one of the prevalent causes of mortality. It was projected that estimated 18.1 million individuals was diagnosed with cancer, and deaths due to cancer increased to approximately 10 million in 2020, according to the International Agency for Research on Cancer (IARC) GLOBOCAN data release (excluding non-melanoma skin cancer) [1]. Cancer morbidity and mortality could be avoided if cancer is detected at an early stage. This is highly important not only for prognosis but also for patient stratification and treatment strategy. Conventional methods such as positron emission tomography, magnetic resonance imaging, and computed tomography are widely used for cancer diagnosis [2]. However, first-line healthcare premises cannot access these necessary devices due to high capital and operational expenses.

In recent years, microfluidic platforms have attracted the attention of doctors and researchers for the purpose of diagnosis. Microfluidic technologies enable the manipulation of fluids under precise and repeatable conditions and offer well-controlled operations in a small scale, which offers an advantage for the detection or isolation of bioparticles. Circulating Tumor Cells (CTCs) have enormous potential as biomarkers for early cancer diagnosis, prediction, and prognosis [3]. Detection of CTCs migrating from primary tumors into the bloodstream has received more attention during recent years because they assist in the early detection and cancer therapy of patients [3]. Previous studies reported the existence of CTCs in the early stages of the cancer and associated it as an indication of the disease progression [4]. Several studies stated that early CTC detection is a promising sentinel of tumor development [5–7]. Different CTC technologies were developed to detect, enumerate, or isolate these rare cells [5]. The key features of a CTC analyzer device are repeatability, reliability, rapidity, cost efficiency, sensitiveness, and user friendliness, which must be addressed before commercialization. The main challenge is that CTCs are rare cells, whose incident number in the peripheral blood circulation compared to other hematologic cells is $10^{-3}/10^{-5-9}$ in mL [5,6,8]. To address this problem, CTC technologies employ two

different strategies involving immunoaffinity and biophysical properties of CTCs. Immunoaffinity utilizes the presence of distinct protein biomarkers such as EpCAM (Epithelial Cell Adhesion Molecule) on the surface of the target cancer cells to capture them onto a desired location [5]. CellSearch® system is the only Food and Drug Administration (FDA) approved positive enrichment immunoaffinity technology so far for some cancer types such as breast, prostate and colorectal cancer and separates the CTCs magnetically using the functionalized ferrofluid nanoparticles coated with EpCAM antibody. However, levels of EpCAM protein expression on the CTCs vary, and the CTCs expressing low-level EpCAM could be lost during the enrichment process [9]. On the other hand, label-free techniques including filtration, centrifugation, streamline sorting, and dielectrophoresis, which are based on biophysical properties of CTCs including size, deformability, density, and polarizability, have been investigated in the literature [10–12]. For example, Sollier *et al.* reported that the size of CTCs collected with a label-free microfluidic device ranged from 12-25 μm in diameter, while this amount for leukocyte was 2-14 μm [10]. Although size-based collection or detection approaches could have disadvantages such as low purity, clogging, limited volume, vortex technology provides screening in a short time, high purity, and application availability in different cancer types. Furthermore, ApoStream® is a system based on the dielectrophoresis technology and utilizes the difference of electrical response of various cells depending on the composition and morphology of the cell type [13]. This system is able to test a 10 mL sample within an hour while capturing viable cells for post processing analysis [5]. There are also new methods for CTCs detection or isolation, which are under investigation and development such as direct imaging modalities [14].

Although many approaches have been used for cancer treatment, one of the procedures is drug delivery through membrane permeabilization. Permeabilization of the cellular membrane is a common biological approach for delivering desired molecules into the cell. Several methodologies [13–16] have been proposed to create pores on the cell membrane. The microinjection method was implemented by injecting the molecules through cells using glass capillary micropipettes [17]. On the other hand, the microinjection approach has significant constraints, including the need for highly qualified technical employees [16]. In another procedure, namely chemical poration,

chemical inducement generates holes on cell membranes. Nevertheless, the specific cellular uptake of the cells and toxic components of the reagents might cause chemical poration, which is practically unavailable [18]. Furthermore, spatial, and temporal control over the process is challenging to achieve.

1.1.1. Cavitation

Cavitation is a process of nucleation, growth, and collapse of bubbles filled with vapor or gas. When the static pressure drops below the saturation vapor pressure of the liquid, cavitation bubbles appear. In hydrodynamic cavitation (HC), the rapid pressure drop can be accomplished within a device containing a flow restrictive element called an orifice or nozzle. Cavitation inception occurs when the first bubbles appear inside the flow restrictive element, and the local pressure, at which cavitation incepts, is called the "Cavitation Inception Pressure." Nucleation on both the macro- and micro-scales is given considerable attention in the relevant basic research. Nucleation could be divided into two groups: homogeneous and heterogeneous. Although it is homogeneous nucleation (induced by thermal motion), which causes the generation of the bubbles from the microscopic voids within the medium, the impurities and weakness points at the boundaries or within the liquid, acting as the features of heterogeneous nucleation, substantially affect the inception pressure [15]. In terms of providing information about cavitation inception of the fluids, studying the mechanism of heterogeneous nucleation in cavitation with impurities is an essential approach.

From a thermodynamical point of view, both co-existing phases (liquid-gas) on the saturated liquid-vapor state possess the same chemical potential state representing two limiting forms of a single amorphous state, where each of the phase changes to the other one through an isothermal volumetric change. According to pressure-volume phase diagram for a pure liquid, whenever there exists an adequate number of nucleation sites with a proper size, the transition of liquid phase to vapor phase takes place, while the pressure is reduced. When a liquid at constant temperature reaches the saturated vapor pressure, a further drop in pressure is required for supplying the liquid molecules' rupture energy to turn into vapor. From a macroscopic point of view, intermolecular forces could be interpreted as surface tension, which keep the molecules tight preventing the evolution of large voids. Considering a constant temperature for a pure

vapor bubble in a liquid, under equilibrium conditions, the exterior liquid pressure is calculated as [16]:

$$P = P_v - \frac{2S}{R} \quad (1)$$

P_v ($\frac{kg}{ms^2}$) is the saturated vapor pressure at the given temperature, S ($\frac{kg}{ms^2}$) is the surface tension, R (m) is the bubble radius, and P ($\frac{kg}{ms^2}$) is the pressure of the liquid exterior to the bubble. If the exterior pressure P becomes slightly smaller than that in Equation (3), the bubble will grow until it reaches a critical radius, where the rupture occurs [16]:

$$\Delta P_c = \frac{2S}{R_c} \quad (2)$$

Wherein, ΔP_c ($\frac{kg}{ms^2}$) is the tensile strength of the liquid, R_c is the critical radius of bubble. Considering a surface tension of $S = 0.05$ ($\frac{kg}{s}$) and a critical bubble size of 10^{-10} (m) pertinent to the intermolecular distance, ΔP_c is in the order of -10^9 ($\frac{kg}{ms^2}$).

However, liquids never withstand such tensions and would yield at pressures several hundred orders smaller than the theoretical one because liquids start to lose their integrity at locations. For heterogeneous nucleation, since the voids are originated at the interface of the liquid/solid/vapor intersection of the suspended particles or channel wall, the contact angle of the bubbles plays an important role in the tensile strength. The tensile strength of the liquid for a heterogeneous nucleation is evaluated as [16]:

$$\Delta P_c = \frac{2S \cdot \sin\theta}{R_c} \quad (3)$$

wherein θ is the contact angle at the interface of the liquid/solid/vapor intersection and is a value representing the hydrophilicity or hydrophobicity of the surface. For the values other than $\pi/2$, the tensile strength in heterogeneous nucleation is less than that of homogeneous nucleation. This reduction in tensile strength at the boundaries of the channel wall and suspended particles turns them into the potential cavitation bubble nucleation sites, which are called ‘surface nuclei’ and ‘stream nuclei’, respectively. The cavitation number is a dimensionless number used to express the intensity of the cavitating flows and can be calculated with the following expression:

$$\sigma = \frac{(P - P_{vap})}{\frac{1}{2}\rho V^2} \quad (4)$$

where P refers to the reference pressure (in this case, it is upstream pressure), ρ is the density of the liquid, and V is the fluid velocity in the constriction zone.

1.1.2. *Micro-scale Cavitation*

Cavitation phenomenon could be resulted in undesired effects such as erosion, and catastrophic damage in conventional scale. The cavitation-on-a-chip approach allows precise control over cavitation phenomenon on a micro-scale due to advancements in the field of microfluidics. Cavitation, where the overall process and the bubble collapse are under control, could be favorable on a micro-scale. Moreover, biomedical and industrial applications could take advantage of micro-scale cavitation [17]. Cavitation in micro and macro scale are different in several aspects. As Mishra et al. concluded at their article [18] the differences of cavitation for micro- and macro-scale are that there is a dominant size scale effect considering the low inception cavitation number for micro-scale cavitation. In addition, choking effect is only dependent on the presence of stream nucleus and their residence time at micro scale cavitation in which the transition from nucleation to choked flow is faster. One of the differences between micro-scale and macro-scale cavitation is constituted by reason of the surface characteristics [19], which is one of the factors significantly affecting cavitation phenomenon. Furthermore, viscous forces and surface tension are the parameters that impact establishing differences between different scales [20]. Hence, the factors determining the nucleation mechanism in the micro platforms include the surface characteristics, device geometry, and flow behavior.

1.1.3. *Micro-scale Cavitation in biomedical engineering*

1.1.3.1. Cell Lysis, Deformation and DNA extraction

Cell-lysis is an essential step in biomolecular analysis where the cell membrane is mechanically or chemically disrupted to release intracellular contents such as protein, DNA, and RNA [21]. Therefore, it is crucial in molecular science, point-of-care diagnostics, protein purification, and drug screening [21]. Microfluidic devices operate in the same scale as cellular dimensions, thereby enabling the investigation of single

cells. Various existing techniques for lysing cells in micro-scale are categorized into four types: mechanical lysis, thermal lysis, chemical lysis, and electrical lysis [22]. Cavitation could possess various impacts on the cell through lysis. A significant amount of mechanical energy is released upon the collapse of a cavitation bubble as a shockwave. Due to the enormous intensity of the shock wave, it has been employed to destroy the cell membrane [21]. A notable superiority of the rapid lysis mechanism is the immediate elimination of all metabolic processes by destroying the cell quickly. Cavitation-enhanced or cavitation-induced cell lysis is an effective process to rupture the cell membrane and extract the cell component [21]. As an example, Liu et al. [23] designed a microbubble array that permitted the rapid lysis of human breast cancer MCF-7 cells through shear stress generated by oscillating microbubbles. The oscillating microbubbles were stimulated with the same frequency, allowing for the efficient release of intracellular compounds from single cells. Additionally, when the input voltage and sonication period were increased, the effectiveness of lysis increased. The microbubble array generated shear stress on the bubble surface and led to the destruction of the targeted cell's membrane with the efficiency of 97.62%. That microbubble array system consumed one minute for cell lysis, while a conventional technique required 15 minutes. As a result, a stable cavitation microbubble array offered a considerably faster and effective lysis than commercial methods for diagnostics and pre-treatment of biological samples. Fast and effective cell lysis is required in numerous Lab on a Chip (LOC) devices to achieve further analysis. Accordingly, Quinto-Su et al. [24] achieved cell lysis in a PDMS microchannel within a time period of nanoseconds to microseconds by taking the advantage of pulsed laser microbeams including flexibility and sheer speed, which allowed microbeams to be directed to any desired location within a short time. Cavitation could be classified into four types based on its method of generation: optic cavitation (OC), acoustic cavitation (AC), particle cavitation (PC), and hydrodynamic cavitation (HC) [25]. In addition to optical cavitation such as laser-induced cavitation, there are cell lysis studies with the use of acoustic and hydrodynamic cavitation [26–28]. Tandiono et al. [29] described a method for lysing microbial cells in a PDMS microchannel by utilizing acoustically induced cavitation microbubbles. The oscillating bubbles produced high shear stress, damaging and destroying *Escherichia coli* (bacteria) and *Pichia pastoris* (yeast) cells. However, according to some experimental and numerical studies, HC is a more

energy-efficient method for cell rupture compared to AC[30]. Furthermore, it was reported that HC consumed approximately an order of magnitude less energy than AC [29]. Biomedical and biomedicine applications of HC in micro-scale constitutes an emerging research direction, which could be realized with low cost and simple experimental setup [27,29]. Gevari et al.[31] investigated diagnostic implementation of HC, which demonstrated that hydrodynamic cavitation bubbles lead to different effects and types of deformation on different types of immobilized cancer cell lines. In another study, Kaba et al. [32] advanced magnetic-bead-based dynamic solid phase extraction (dSPE) of DNA and chemical lysis by using a laser-machined polycarbonate microfluidic chip, which generated cavitation microstreaming. Strong circulatory flows surrounding bubbles produced agitation, quick lysis as well as DNA extraction and purification. Molecular interaction made DNA bond the magnetic beads under high-ionic-strength chemical activating circumstances. Within a short assay time (25 minutes), high extraction efficiency (76.9%) and purity ($A_{260}/A_{280} = 1.85$) were attained from a very diluted cell sample.

1.1.3.2. Cell Membrane Permeabilization, Drug delivery

Controlled drug delivery and release are critical in evaluating the biological response stimulated by external factors to assist drug transportation, which is complicated in *in vivo* implications. Microfluidic technologies enable manipulation of fluids and investigation under precise and repeatable conditions and offer well-controlled operations in small scale, which enhance the drug delivery performance and provide a better understanding about fundamental transport processes facilitated by membrane permeabilization [33,34]. In this regard, Hellman et al. [35] demonstrated that cell lysis and molecular delivery were accomplished in confluent monolayers of adherent PtK2 cells using 6 ns, $\lambda=532$ nm laser microbeam irradiation. The biophysical effects of the plasma formation, cavitation bubble generation, expansion, and collapse on cells upon laser beam irradiation were observed. Furthermore, the authors were able to identify and quantify regions of immediate cell lysis, cell necrosis, and molecular delivery in cell monolayers cultured at a density of 1000 cells/mm² using cell viability and membrane permeability assays to determine the region of optimum shear stress for optoporation molecular delivery. Remarkably, the study highlighted the importance and critical consequences of cavitation bubble expansion generating the shear stress effect on cell

lysis, cell viability, and molecular delivery. The authors demonstrated that the cells exposed to a maximal wall shear stress $tw_{,max} > 190 \pm 20$ kPa were instantly lysed, while the cells subjected to $tw_{,max} > 18 \pm 2$ kPa became necrotic and detached. The cells exposed to $tw_{,max}$ values between 8 and 18 kPa were viable and effectively optoporated with Dextran molecules of 3 kDa. When the cells were exposed to $tw_{,max} < 8 \pm 1$ kPa, they remained viable without molecular uptake. Pulsed laser microbeams offer the advantage of cavitation bubbles with consistent size and placement, thereby leading to reproducible regions of cell lysis, optoporation, and viability. The majority of prior sonoporation and optoporation research studies employed a population of microbubbles [36,37]. Unlike numerous microbubbles, in the study of Le Gac et al. [38], a single laser-induced cavitation bubble was preferred to sonoporate HL60 (human promyelocytic leukemia) suspension cells in a microfluidic chamber to achieve better control of bubble effect. The membrane poration of cells was determined by the calcein release from calcein-loaded cells or trypan blue uptake of the cells. Cavitation bubbles were shown to have elicited membrane poration in cells in their close area. When the non-adherent cells were positioned to a region with more than four times the maximum bubble radius (R_{max}), they maintained their physical properties, whereas the membrane commenced to porate when the cells were located closer than $0.75 R_{max}$. Therefore, the results indicated that flow-induced poration of suspension cells are applicable to lab-on-a-chip platforms. In another study, Li et al. [39] designed a highly controllable system with a laser-induced single microbubble to form a microjet within a microfluidic chip and single-cell trapping configuration, which led to poration of the membrane of a single suspension cell. The trapping configuration operated as rigid boundaries, triggering the microjet necessary for cell membrane poration. Microjetting occurred due to the irregular expansion and collapse of the cavitation bubble alongside the cell, which ruptured and porated the cell membrane. The experiments determined the membrane integrity of the myeloma cell using trypan blue uptake, where the trypan blue uptake increased while the distances were decreased. This approach enabled rapid, consistent, and targeted destruction of single cell membrane in suspension. Stable cavitation obtained with low acoustic pressures promotes acoustic microstreaming with acoustic effect in an aqueous-fluid environment. However, inertial cavitation achieved with a microjet with a higher acoustic pressure (along with the formation) vigorously generates shock wave emission. Stable cavitation induced fluid

phase/receptor-mediated endocytosis to stimulate uptake of the macromolecule. However, inertial cavitation resulted in the temporary membrane pore formation, Ca²⁺ rush into the cell, and subsequent lysosome exocytosis that facilitated the entrance of other macromolecules [40]. Meng et al. [36] provided an approach to perform sonoporation in a more efficient and controllable manner with a stable microbubble array. The study described a methodology for adjusting membrane permeability by utilizing a microfluidic device and an oscillating microbubble array allowing for self-repairable sonoporation. Multiple rectangular channels were fabricated on the sidewall to produce an array of monodispersed microbubbles, which were triggered with the same frequency to assure homogeneity in terms of microbubble size. Surface tension led to a microbubble array with bubbles of the same size while the fluid flowed inside the channel. Single cells were confined at the bubble surface due to the combination of the drag force and secondary acoustic radiation force. Single oscillating microbubbles created shear stress on the membrane, its permeability changed. Homogeneous and controllable sonoporation was achieved with parallel microchannels. The development of such systems providing more controlled poration via cavitation is a favorable technique for the transportation of molecules and drugs through the cell membrane while maintaining the cell viability.

1.1.3.3. Blood-Brain-Barrier

Organ-on-a-chip systems offer a platform, which allows for the evaluation of on-target and off-target effects of the drugs and effectiveness of drug delivery by emulating the physiology of the biologic structure [41]. In this fashion, more controlled systems could be developed in micro scale, and accelerated pre-clinical drug screening could be achieved [41,42]. Blood-brain barrier (BBB) is an active diffusion barrier connecting the Central Nervous System (CNS) to the body to control the crossing of molecules and eventually maintain homeostasis. BBB-chip models were designed to biomimic transportation of metabolites and nutrients to the brain cells and to inhibit the pathogenic and toxic substances [43,44]. The development of such microchips is crucial in manipulation of cells under *in vitro* co-culture condition and *in vivo* microenvironment in both forms of 2D or 3D [45]. BBB is formed by brain microvascular endothelial cells (BMECs), which are key components for microvasculature. Many research studies investigated and developed drug delivery

systems considering the endothelial barrier [46–48]. Therefore, targeted drug delivery through the endothelial barrier is highly required. Cavitation facilitates drug delivery through reversible and transitional weakening between endothelial cells junctions. This technique, known as USMB-mediated drug delivery, included microbubble injection (MBs) combined with ultrasound exposure [40]. The USMB is a safe and promising method, which potentially evades physiological-induced barriers' irreversible destruction [40]. Silvani et al. [49] showed the reversible opening through protein junctions with the utilization of a cavitation-enhanced permeabilization system. Hence, the impact of microbubbles on the endothelial barrier was observed and assessed through a designed vessel-on-a-chip mimicking BBB. Microbubbles were revealed to intensify the ultrasonic impact, resulting in the inter-endothelial gaps and subsequent barrier permeabilization. Compared to the control case, the gap area expanded considerably with increasing pressure amplitude. The gap area (opening) reverted to the control level (initial) after insonication, demonstrating that the process was completely reversible. The fabrication of microfluidic platforms based on the biochemical and geometrical properties of the actual biostructure could be a potential for analyzing the effect of cavitation microbubbles on the cell and biological structure.

1.1.3.4. Cell Sorting/Focusing

Different microchannels and microfluidic systems have been widely engaged in biomedical applications, DNA purification, biological analysis, and polymerization for mixing and sorting purposes [50–53]. Various methods were proposed using the advantages of cavitation, such as high purity and speed in micro-scale for sorting purposes. As an example, Wu et al. [54] reported a high-throughput 3D microfluidic cell sorting system (PLACS) utilizing pulsed laser-induced cavitation bubbles, which generated 3D sheath flows by high-speed liquid jets. In the enrichment mode, the fluorescence-activated cell sorter achieved 45% sorting purity, and 45 000 mammalian cells per second. In the high purity mode, it achieved 90% purity at 23000 cells per second. Nonetheless, experiments could suffer from channel blocking and need high pressure to push the fluid into the channels. To avoid this issue and to reach high-throughput, Chen et al. [55] designed a single layer PDMS channel, which enabled an inertial focusing combined sheathless PLACS for cell sorting. Mammalian cells demonstrated more than 80% purity for 6000 cells per second, and beyond 90% for

10000 particles per second.

1.2.Motivation and Novel Aspects

Although macro-scale hydrodynamic cavitation has a very destructive effect due to the high released energy from the cavitation bubble explosion, damaging effects of cavitation could be minimized and utilized for biomedical applications through micro-scale HC inside a microfluidic device. Microfluidic technologies enable the manipulation of fluids under precise and repeatable conditions and offer well-controlled operations in a small scale, which offers an advantage for the detection or isolation of bioparticles. Early cancer diagnosis and effective therapeutic technologies appear to be inevitable needs for the human health. Although various devices have been designed to detect, enumerate, and isolate CTCs from blood, some of these devices could have some drawbacks, such as the requirement of labeling, long process time, and high cost. While HC has been proven as a versatile phenomenon in the biomedical applications, the detection of CTCs based on HC inception has not been investigated so far in microfluidic devices. To this end, first part of this study aims to present a microfluidic device based on the novel concept, “Hydrodynamic Cavitation on a Chip (HCOC),” which can detect CTCs in the order of minutes by utilizing interfaces between roughness elements on chip and cells. The HCOC microfluidic device could be an alternative method and could detect the presence of CTCs and offer a cheap, user-friendly and rapid tool, which does not require any biomarker or a biosensor. The HCOC possesses straightforward application procedures to be employed for detection of CTCs. While bio-related applications such as cell lysis and cell permeabilization have been carried out by utilizing acoustic and optical cavitation until now, a limited number of studies have been reported on biomedical applications of HC. The HCOC offers the advantage of creating well-defined zones of bio responses upon HC exposure within minutes, achieving cell lysis and molecular delivery through permeabilization by providing spatial control. HC proposes a promising alternative to the existing technologies by increasing the therapeutic efficacy of anticancer drugs. This approach has the potential to be easily integrated to clinical and *in vivo* studies, in the near future.

1.3.Thesis Objectives

This study aims to investigate and analyze the role of the HC on circulating tumor cell (CTC) detection and cancer treatment by *in vitro* studies by revealing the biophysical effect of HC in an HC-on-a-chip device (HCOC) (cascade parallel multi-microchannel device). Two studies present an investigation of cancer diagnosis (CTC detection) and analysis of cancer treatment based on hydrodynamic cavitation:

- Hydrodynamic cavitation on a chip as a cancer diagnostic tool (CTC detection):
 - Cavitation inception of different working fluids
 - Relationship between cavitation inception and cell concentration- (CTC Enrichment)
 - Cavitation Inception of Blood Sample

- Cancer treatment using facile hydrodynamic on a cascade device:
 - Characterization of the zones of cellular response
 - Characterization of the morphological changes after HC exposure
 - Fluorescent examination of live/dead cells by Calcein AM/PI staining
 - Demonstration of cellular uptake upon HC exposure
 - Changes in cell viability after HC + DOX treatment
 - Effect of the HC on biomechanical properties of the cells

2. CHAPTER TWO: HYDRODYNAMIC CAVITATION ON A CHIP AS A CANCER DIAGNOSTIC (CIRCULATING TUMOR CELL DETECTION) TOOL

2.1. Research Objectives

Circulating tumor cells (CTCs) are essential biomarkers for cancer diagnosis. Although various devices have been designed to detect, enumerate, and isolate CTCs from blood, some of these devices could have some drawbacks, such as the requirement of labeling, long process time, and high cost. This study presents a microfluidic device based on the novel concept, “Hydrodynamic Cavitation on a Chip (HCOC),” which can detect CTCs in the order of minutes by utilizing interfaces between roughness elements on chip and cells. The working principle relies on the differences in cavitation inception of the working fluids through the microfluidic devices with roughness. Three experimental groups, cell culture medium, medium+Jurkat cells, medium+Jurkat cells+ CTCs and medium+ CTCs were utilized as the working fluids in the fabricated microfluidic device. Here, Jurkat cells were used to mimic white blood cells and MDA-MB-231 cells were spiked into the medium as CTCs. Accordingly, the group with CTCs led to detectable earlier cavitation inception. Additionally, the effect of the CTC concentration on cavitation inception and the effect of the microfluidic device wall roughness were evaluated in terms of interfaces between roughness and cells were evaluated. Furthermore, CTC detection tests were performed with cancer cell lines spiked in blood samples from healthy donors. The results show that this approach, HCOC, could be an alternative method and could detect the presence of CTCs based on cavitation phenomenon and offer a cheap, user-friendly and rapid tool, which does not require any biomarker or a biosensor. The HCOC possesses straightforward application procedures to be employed for detection of CTCs.

2.2. Experimental Method

2.2.1. Cell Culture Sample Preparation

Studies have shown that Jurkat cells are most similar cell line to leukocytes in terms of size and elastic properties. Therefore, Jurkat cells are widely used to mimic white blood

cells in the studies involving CTCs [56,57]. In this study, human breast adenocarcinoma cell line MDA-MB-231 [American Type Culture Collection (ATCC) number HTB-26] (for mimicking CTC) and Jurkat human acute T lymphocyte leukemia cell line (ATCC-Clone E6-1 number TIB-152) [for mimicking white blood cells (WBC)] were employed. Roswell Park Memorial Institute Medium 1640 (RPMI 1640, P04-17500), Dulbecco's Modified Eagle Medium (DMEM, P04-03500), Fetal Bovine Serum (FBS, P30-3306) for cell culture were purchased from PAN-Biotech (Aidenbach, Germany). Penicillin-Streptomycin Solution, L-Glutamine, Trypsin EDTA Solution C (0.5%) were obtained from Biological Industries (Beit HaEmek, Israel). MDA-MB-231 cells were cultured in DMEM, whereas Jurkat cells were cultured in RPMI 1640. Both basal cell culture media were supplemented with 10% heat-inactivated Fetal Bovine Serum (FBS), 100 units/mL penicillin, 100 µg/mL streptomycin, and 100 µg/mL L-glutamine. 100x non-essential amino acids MEM-NEAA solution (Gibco, 11140035) was also added into DMEM. Cells were incubated at 37°C in a 5% CO₂ humidified incubator. When the confluency of MDA-MB-231 cells was reached to 90%, cells were passaged after detaching from the surface with 0.25% trypsin/EDTA solution. Since Jurkat cells are non-adherent, they were passaged with fresh medium in appropriate proportions without trypsin treatment. The number of dead cells was measured by using trypan blue before each experiment and live cell percentage was always kept above 95%. Unless the live cell concentration was lower than 95%, the removal of dead cells with centrifugation was not applied. Four experimental sample groups were prepared (Figure 1): first group contains only medium (RPMI 1640), while second group contains Jurkat cells within the medium (Jurkat group), third has Jurkat cells and cancer cell line (Jurkat+CTC group) and the last one contains Jurkat cells+ cancer cell line (CTC group). There is 200 mL of RPMI 1640 medium in the no cell containing group. For Jurkat cell group, the concentration of Jurkat cells were adjusted to 1×10^6 cells/mL in a total of 200 mL. The CTC concentration was 300 cells/mL in a total of 200 mL medium. Similarly, the Jurkat+CTC group was prepared in a 200 mL of total cell culture volume with Jurkat cell concentration 1×10^6 cells/mL and CTCs concentration 300 CTCs/mL. The same procedure was followed for different concentration tests using 1×10^6 cells/mL Jurkat cells and 100 CTCs/mL, 50 CTCs/mL, respectively. The confluency of CTCs cultured in DMEM was as high as $1-2 \times 10^6$ / mL. Therefore, a very small volume of DMEM containing CTCs needed to be added into RPMI 1640 to obtain 300 CTCs per mL in

RPMI. At the end, the percentage of the DMEM volume in RPMI was approximately 0.001%, which was less than the error of the detection system. Hence, the amount of DMEM including cancer cells did not impact the measured cavitation inception of the group with CTC added in RPMI 1640.

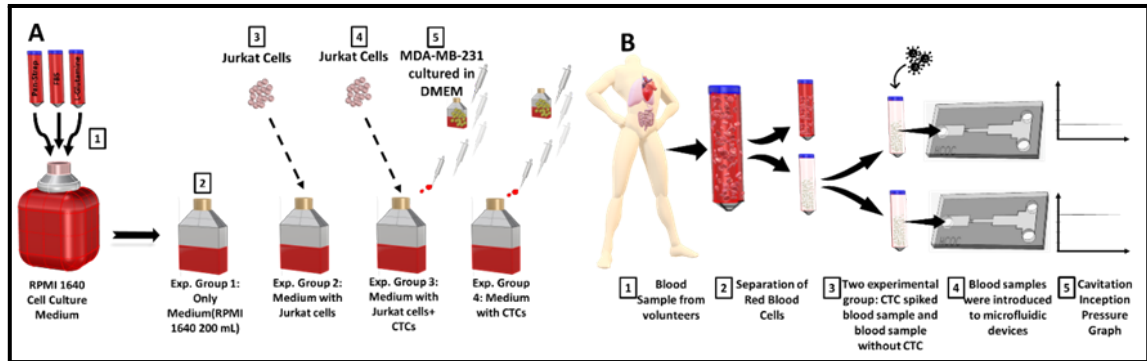


Figure 1: A) Schematic of cell culture preparation before the experiments and B) blood sample preparation before cavitation tests. A.1) The group including only RPMI 1640 cell culture medium, A.3-4) adding Jurkat cells on a flask, A.5) seeding MDA-MB-231 cells, cultured in DMEM previously, on a flask. B.1) Blood samples were collected from volunteers into sample tubes. B.2) Red blood cells were lysis, centrifuged and discarded. B.3) Remaining samples divided into two groups considering cell concentration and CTCs were spiked into one of the groups. B.4) Each sample were introduced to different microfluidic devices with exactly same configuration. B.5) Cavitation inception pressures were recorded for each group and graphs were plotted.

2.2.2. Blood Sample Preparation.

The study protocol was approved by Yeditepe University KAEEK (2012-KAEEK-70). Blood samples were collected from healthy volunteers into vacutainer tubes containing the anticoagulant EDTA. After completing cell culture tests, processed blood samples were divided into three groups considering cell number per mL. Blood sample of first (N1) and second group (N2) do not include CTC and were collected from different volunteers, which resulted in different blood characteristics. While blood sample of the second and the third group were collected from the same volunteers. The second group does not contain any CTCs while third group contains CTCs. Peripheral blood samples (10 ml in K-EDTA) were diluted 1:3 with 1X Red Blood Cell Lysis Buffer (87,4 gr/l NH₄Cl, 10 gr/l KHCO₃, 1 mM EDTA for 10X Lysis Buffer stock). The mixture incubated at room

temperature for 10 minutes with gentle shaking. Then it was centrifuged at 2000 rpm for 10 minutes and repeated twice with the above-mentioned buffer to remove all red blood cells. White blood cells; including PBMCs, monocytes, T and B lymphocytes, were obtained and resuspended with RPMI. Cell concentrations per ml were counted using Thermo Fisher Countess II Automated Cell Counter.

2.2.3. Microfluidic Device Design, Fabrication and Experimental Procedure

2.2.3.1. Fabrication Method and Device Configuration

The microfluidic device consists of a patterned silicon wafer substrate bonded by a glass lid for the sake of visualization. The process flow to fabricate the device is summarized in this section and represented in figure 2. The thickness of the AZ-ECI photoresist used in photolithography was 2 μm , and the energy required for this thickness in photolithography was 320 mJ/cm^2 . After this step, the photoresist remaining on the surface was removed with a resist stripping step. In the second lithography process, a 2 μm thick photoresist was applied, and dry etching was followed to etch the SiO_2 layer by a second photomask for opening the inlet, outlet, and channel. Afterwards, the deep reactive ion etching (D-RIE) procedure was applied to etch the substrate along a distance up to 330 μm . The coated resist was removed entirely in this step. Then, the etching process continued with the bottom side of the substrate. However, before the second D-RIE, the silicon substrate was coated with 2 μm Ti and Al layers on the bottom side so that the sample wafer could withstand applied stress in etching. Subsequently, residual SiO_2 and Al, Ti layers were eliminated by wet etching process. In the final step, the silicon substrate was bonded to Borofloat-33 glass by anodic bonding.

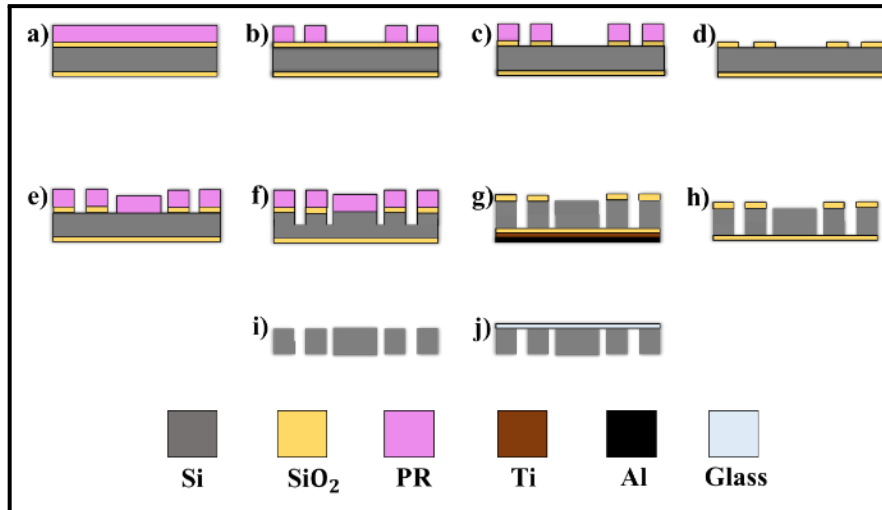


Figure 2: a) Photoresist casting on a silicon dioxide-coated wafer. b) Lithography with photoresist coating for channel design. c) SiO₂ etching, d) photoresist removal, e) Lithography for the inlet–outlet and pressure ports. f) DRIE for Si to open inlet-outlet and pressure ports. g) Resist stripping and Ti, Al coating also DRIE for etching through the wafer h) Wet etching of Al and Ti. i) Wet etching of SiO₂. j) Anodic bonding of the silicon wafer to glass.

The microfluidic device (HCOC) used in this study mainly consists of an inlet, microchannel and extension part designed on a silicon wafer (Figure 3). A pressure port is extended into the inlet region just upstream the microchannel’s entrance. The flow entering the device through the inlet encounters the microchannel, passes through the channel, and continues through the extension part. When the working fluid reaches the microchannel, which has a narrower cross-sectional area compared to the inlet region, a sudden pressure drop occurs at the vena-contracta region of the microchannel inducing cavitation inception. Finally, the fluid reaches the exit and leaves the microfluidic device. In this study, two microfluidic devices with same configuration and different roughness properties were used. First device has no surface or sidewall roughness (Chip-wo-R), while the second device has sidewall roughness (Chip-R). The total length of both microfluidic devices is 6000 μm . The width of the inlet region as well as the outlet region of the devices are 900 μm , and the microchannels’ width are 300 μm (Table 1). In our previous studies, we observed that lateral roughness structures of microfluidic device affected cavitation inception) [58]. Thus, the microfluidic devices designed and fabricated for this study also possess sidewall roughness elements. In

order to compare roughness elements on cavitation inception, two microfluidic devices were used. While both devices have the same configurations, one has a roughness, and the latter device has no lateral sidewall roughness [58,59].

Table 1: The geometrical properties of the microfluidic device without roughness (Chip-wo-R).

Physical Configuration (Chip-wo-R)	Range
Microchannel length (L_n)	2000 μm
Microchannel width (W_n)	300 μm
Microchannel depth (h)	100 μm
Outlet region length	2000 μm
Outlet region width	900 μm
Length of the roughness elements (L_R)	0
Height of the roughness elements (H_R)	0

Table 2: The geometrical properties of the microfluidic device with roughness (Chip-R).

Physical Configuration (Chip-R)	Range
Microchannel length (L_n)	2000 μm
Microchannel width (W_n)	300 μm
Microchannel depth (h)	100 μm
Outlet region length	2000 μm

Outlet region width	900 μm
Length of the roughness elements (L_R)	1 L_n
Height of the roughness elements (H_R)	0.01 W_n

2.2.3.2. Experimental Setup of Microfluidic System (HCOC)

The experimental setup for HC test rig includes a high-pressure nitrogen tank (Linde Gas, Gebze, Kocaeli), liquid container (Swagelok, Erbusco BS, Italy), stainless steel tubes (Swagelok, Erbusco BS, Italy) and chip sandwich (holder). A CMOS high-speed camera (Phantom VEO-710L) with a resolution of 1280x800 pixels and pixel size of 0.02 mm was employed to visualize cavitation inception inside the microfluidic device during tests. A macro camera lens (type K2 DistaMax) with a focal length of 50 mm and a f-number of 1.2 was used. The high-pressure pure nitrogen tank was connected to the container, allowing the liquid inside the container to move through the tubing towards the device. The microfluidic device was connected to the pressurized tubing through a sandwich holder, which has an aluminum micromachined substrate and two transparent plexiglass lids pushing the chip to the substrate by the means of screws shown in figure 3. The sandwich holder has an inlet port, an outlet port, and a pressure gauge port (Omega, the USA with an accuracy value of $\pm 0.25\%$) (shown in Figure 3).

2.2.4. The HC-On-Chip (HCOC) Experiments and CTC Detection Protocols:

2.2.4.1. Cavitation Inception Measurement Procedure of Different Working Fluids

Hydrodynamic cavitation occurs when an upstream pressure large enough to initiate phase change is exerted to the fluid entering the flow restrictive element of the HCOC. The inception cavitation is identified using the shadow-graph technique, which differentiates the emergence of cavitation by high-speed recording of the reflection of the light source over the silicon substrate. At inception cavitation, a dark shadow of the gaseous region at the vena-contracta of the microchannel appears as could be seen in figure 3. Thus, cavitation inception pressure values were assessed based on the measurement of upstream pressure in the inlet region pressure port of the system at cavitation inception. Two pressure gauges at different locations were used to verify the

measurements in order to avoid the errors caused by clogging at the inlet region pressure port. One pressure gauge was located just upstream of the inlet port of the sandwich, whereas the other pressure gauge was connected to the pressure port within the inlet region of the microfluidic chip through the sandwich holder. After each test, the chips were cleaned and were reused for the next trial. DI water test was performed as the reference value for the cleaning procedure before testing the other samples. The samples were introduced to the system by gently infusing them into the liquid container using pipettes. Four experimental groups, namely RPMI 1640, Jurkat, Jurkat+CTC, and CTC were tested. A previously prepared 200 mL RPMI 1640 medium with no cells was tested, and the value for cavitation inception was recorded. Afterwards, the group containing a certain amount of Jurkat cells in 200 mL RPMI 1640 medium was introduced to the system, and the inception cavitation was observed. Finally, the inception pressure of the of the Jurkat cells with the concentration of 300 CTCs/mL in 200 mL RPMI 1640 medium and inception pressure of 300 CTCs/mL in 200 mL RPMI 1640 were recorded. The tests with all the groups were repeated for eight times as biological replicates using a unique unused sample for each trial. After complete sterilization of the experimental setup, blood samples were introduced to the setup, respectively. After each experiment, microfluidic device was change with another device has the same configuration with the previous one. Between each experiment, the setup was cleaned and sterilized. Cleaning procedure was started before the experiments, the container and tubing were washed separately for about ten minutes by passing DI water through them, and the microfluidic device was sonicated for about 15 minutes in acetone before installing the setup. Afterwards, 600 mL of 70% ethanol was passed through the experiment setup at a pressure up to 2.07 MPa. DI water was also passed for three times through the setup at a pressure of 1.38 MPa to remove remaining ethanol. All the above mentioned protocol was repeated after conducting the tests for each experimental group.

2.2.4.2.Cavitation Inception of Medium with Different Number of CTCs

Besides the billions of red blood cells and millions of white blood cells in the blood, CTCs are 1-10 per mL of blood [60]. Therefore, CTCs, which are very rare in the blood, are very difficult to detect. Also, to evaluate the capability of the device in enumerating the number of CTCs, in addition to the cavitation inception pressure of Jurkat + 300 CTCs/mL, the inception pressures of Jurkat+100 CTCs/mL and Jurkat+ 50 CTCs/mL

were also recorded for at least three times. The detection of enriched CTCs (different number of CTCs in mL) was based on hydrodynamic cavitation. In addition to the cavitation inception pressure of Jurkat+300 CTCs/mL, Jurkat+ 100 CTCs/mL and Jurkat+ 50 CTCs/mL were also recorded.

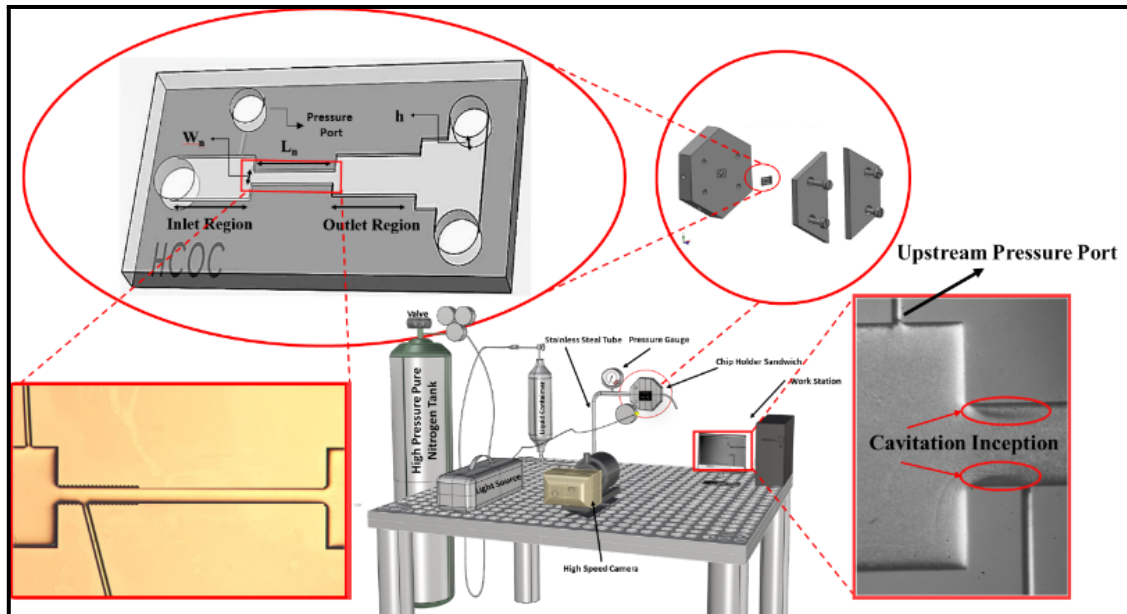


Figure 3: Experimental setup and microfluidic chip details. The cavitation inception is detected using the high-speed camera and the pertinent pressure to the instance of cavitation inception is recorded as the cavitation inception pressure.

2.2.5. Characterization methods. Scanning Electron Microscopy (SEM)

The samples were subjected to an SEM sample preparation protocol as stated in Figure 4 the Scanning Electron Microscopy offered further evaluation on cell morphology including size and shape. The prepared samples were coated with three layers of Au/Pd, and the cells were observed using field emission scanning electron microscopy (FESEM, LEO Supra VP-55). The accelerating voltage was kept under 3kV, and the working distance was in the range of 8 to 10 mm.

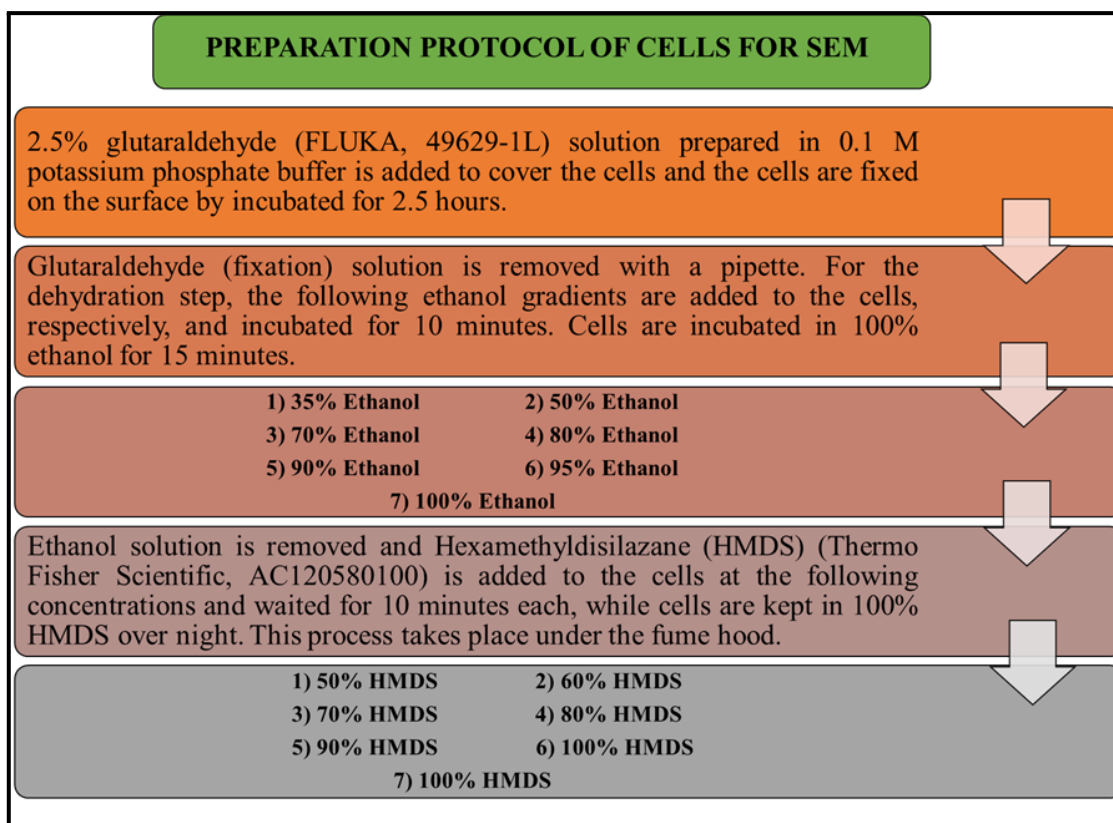


Figure 4: Sample fixation protocol for SEM analysis

2.2.6. Cell Staining

DILC18(3) fluorescent dye (Life Technologies, D3911) was used to stain MDA-MB-231 and Jurkat cells. 2.5 mg of dye was added per mL of Dimethyl Sulfoxide (DMSO) (Santa Cruz, cs-358,801) to prepare a stock solution. The cells were resuspended in PBS (Gibco, 20,012–019) with 3% FBS at a concentration of 1,000,000 cells/mL. Stock dye was introduced at 5 μ L/mL cell suspension ratio. The stained MDA-MB-231 cell line was incubated for 20 min, while Jurkat cell line was incubated for 5 min at 37 °C. Afterwards, the cells were rinsed with PBS until the supernatant became totally clear.

2.2.7. Statistical Analysis

All experiments were conducted at least in triplicate. The mean values, standard deviations and standard error values of all obtained results were reported. Relationships among groups were analyzed using one-way ANOVA (SPSS 12.0, SPSS GmbH,

Germany), [Newman–Keuls multiple comparison test (* $p < 0.05$, ** $p < 0.01$, *** $p < 0.001$)].

2.3.Results

2.3.1. Cavitation Inception

According to the results obtained from the test through the first microfluidic device (Chip-wo-R) without roughness, the RPMI 1640 (control group) was observed to have a high inception pressure compared to the groups Jurkat and Jurkat+CTC. RPMI 1640 gives inception at $0.71 \text{ MPa} \pm 0.02$ while group Jurkat inception pressure is $0.65 \text{ MPa} \pm 0.03$ and Jurkat+CTC is $0.52 \text{ MPa} \pm 0.01$. When the inception pressures of the fluid with Jurkat and fluid with Jurkat +CTC are compared, the inception pressure of the group with CTC exhibits a statistically significant decrease.

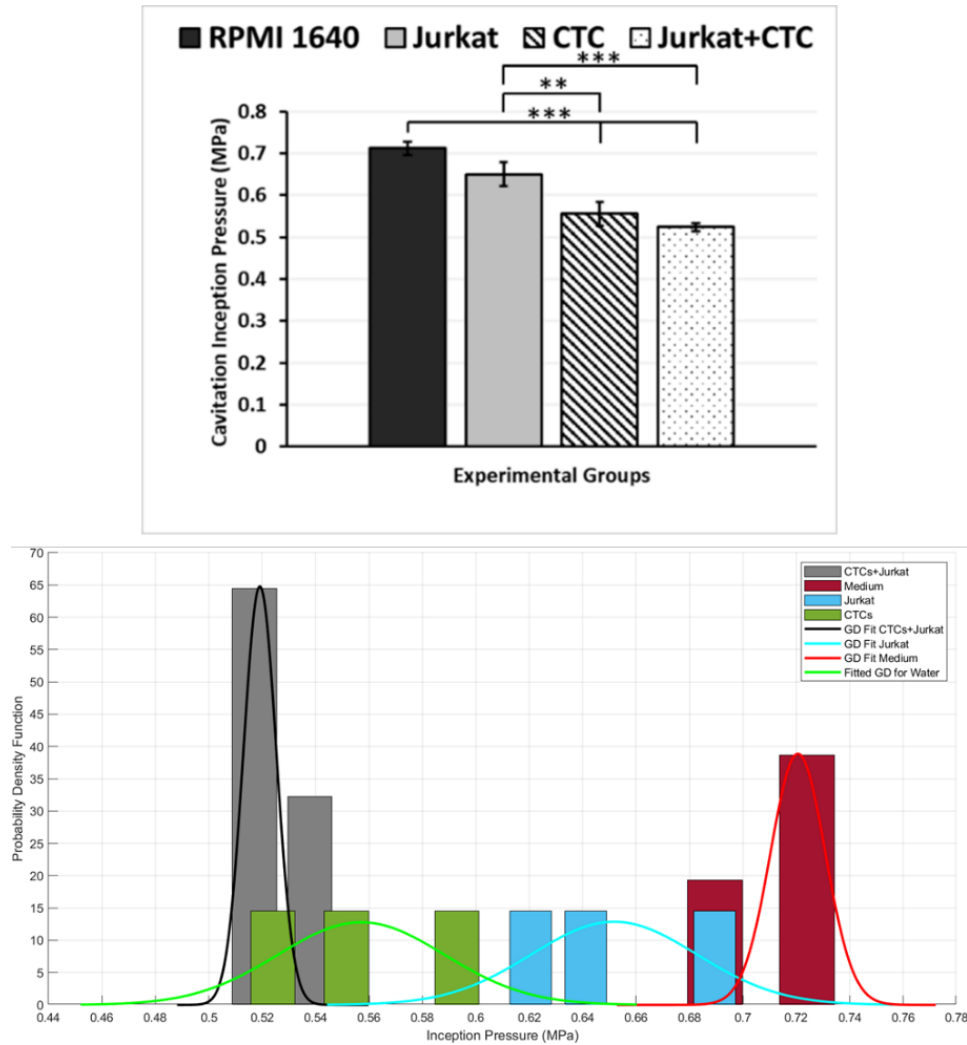


Figure 5: A) The graph shows that cavitation inception pressures of different working fluids through microfluidic device without roughness (Chip-wo-R). The working fluids are RPMI 1640 cell culture medium, Jurkat, CTC and Jurkat+CTC. Error bars indicate standard deviation. **B)** Probability distribution graph of Medium, Medium with Jurkat Cells and Medium with Jurkat Cells+CTCs in terms of cavitation inception pressure. The inception pressure data was derived 8 times for each sample and the nonlinear fit was performed in MATLAB to show the inception pressure for each sample as a Gaussian distribution.

Once the cavitation inception pressures of the different experimental groups are analyzed (Figure 5), it is evident that there is a significant difference between the group containing only RPMI 1640 and the group Jurkat+ CTC. These results prove that when

CTCs are added to the cell medium, the cavitation inception pressure significantly decreases. Thus, the group containing cancer cells can be easily identified. Moreover, the inception pressure of the CTC group is $0.56 \text{ MPa} \pm 0.03$.

Figure 5 B shows the probability distribution of pressure values corresponding to different groups. Accordingly, the pressure range of the group Jurkat+CTC is between 0.5 and 0.54 MPa. The peak pressure value of the group Jurkat+CTC is approximately 0.52 MPa. This pressure value does not coincide with the Jurkat pressure distribution. On the other hand, the interval of Jurkat cells is broader than in the Jurkat+CTC. The peak pressure of the group Jurkat is approximately 0.65 MPa. There is not an overlap area between the intervals of the Jurkat group and the Jurkat+CTC group. Besides, the cell medium interval range is between 0.65 MPa and 0.77 MPa. It is seen that the area where the group Jurkat overlaps with the medium group is significant, indicating that Jurkat cells do not make any striking difference in inception values. However, there is no interval coincidence between group Jurkat+CTC and group medium while there is tiny overlap area between intervals CTC and group medium, which demonstrates groups with CTCs creates noticeable difference.

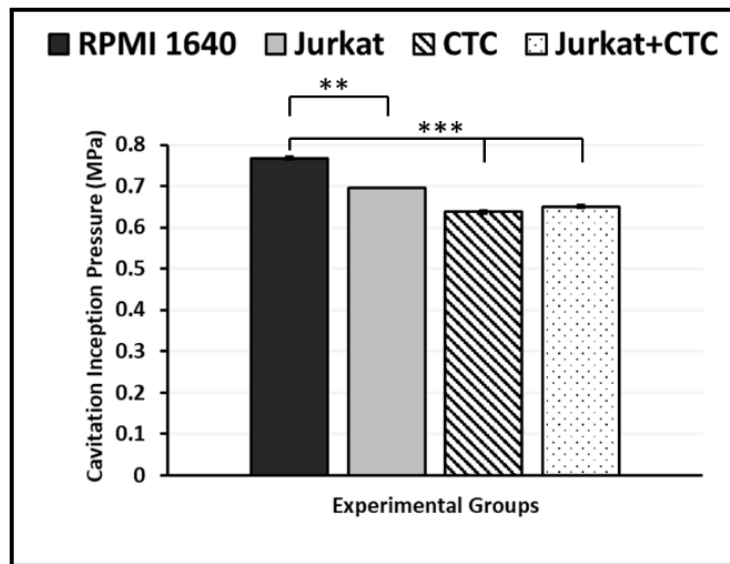


Figure 6: The graph shows that cavitation inception pressures of different working fluids through microfluidic device with roughness (Chip-R). The working fluids are RPMI 1640 cell culture medium, Jurkat, CTC and Jurkat+CTC. Error bars indicate standard deviation.

The microfluidic device (Chip-R) brings about different cavitation inception pressure values from the Chip-wo-R for different working fluids (Figure 6). RPMI 1640 gives inception pressure $0.77 \text{ MPa} \pm 0.02$ while Jurkat inception pressure was $0.69 \text{ MPa} \pm 0.02$. The difference between the RPMI group and other are significant. However, there is no significant difference among Jurkat, CTC and Jurkat +CTC group. The CTC group inception pressure is $0.64 \text{ MPa} \pm 0.003$ and inception pressure is $0.65 \pm 0.003 \text{ MPa}$ for Jurkat+CTC group.

2.3.2. Relationship between Cavitation Inception and Concentration of Cell-CTC Enrichment

Based on the results given in Figure 7, the inception pressure of all groups containing different amounts of CTCs are lower compared to the group containing only Jurkat cells. While the average inception pressure of the group containing Jurkat cells is $0.65 \text{ MPa} \pm 0.03$, the average inception pressures of the groups containing 300, 100, and 50 CTC per mL are $0.52 \text{ MPa} \pm 0.01$, $0.54 \text{ MPa} \pm 0.003$, and $0.59 \text{ MPa} \pm 0.009$, respectively. No significant pressure difference can be observed for the 300, 100, and 50 CTC groups per mL. If concentration of CTCs was over 300 per mL, perhaps the decreasing trend in the inception pressure with increasing CTC numbers could have been captured. Moreover, while 300 CTCs/mL and 100 CTCs/mL have significant difference between Jurkat group, the difference 50 CTCs/mL and Jurkat group is less significant compared to other groups.

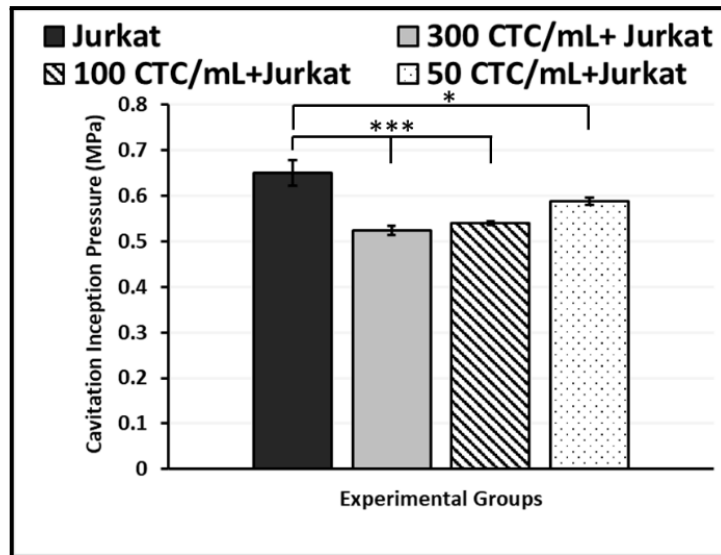


Figure 7: Column graph of the cavitation inception pressure of Jurkat, 300 CTCs/mL +Jurkat, 100 CTCs/mL +Jurkat cells and 50 CTCs/mL+Jurkat cells

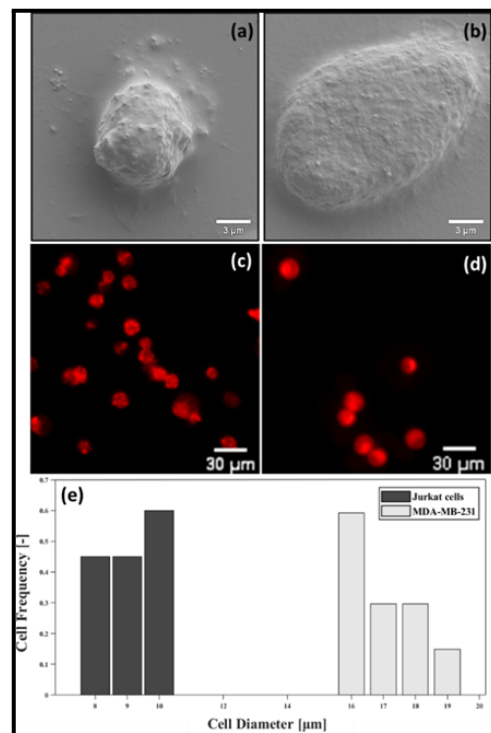


Figure 8: SEM images of (a) MDA-MB-231 cell line (b) Jurkat cell line. Fluorescence microscopy images of the cells after staining Jurkat Cell (c), MDA-MB-231 (d) and size distribution of the Jurkat and MDA-MB-231 cells (e).

The size distribution graph shows that Jurkat cells range from 8 μm to 10 μm and the

obtained sizes of MDA-MB-231 cells range from 16 μm to 19 μm (Figure 8). As a demonstrable proof, the SEM images of Jurkat cells and MDA-MB-231 are shown in Figure 8. A single MDA-MB-231 cell's diameter was measured as 17.9 μm , while the diameter of Jurkat cell was 7.1 μm . The average value of these diameter was obtained by taking measurements from different regions of SEM images of both types of cells. MDA-MB-231 cells, which are approximately three times larger in size, affect the cavitation inception behavior and cause an earlier cavitation inception (at considerably lower upstream pressures).

2.3.3. Cavitation Inception of Blood Sample

According to the results, the inception pressure of the N1 blood sample is 0.87 ± 0.01 , and there of the N2 blood sample is 0.88 ± 0.01 , which there is no significant difference between them. However, CTC-spiked blood sample results in significantly lower inception pressure, which is 0.67 ± 0.02 . The N2 blood sample and the sample with CTC are collected from the same healthy volunteers. Therefore, the concentration and ingredients are considered the same. Especially, in comparison of N2 and CTC-spiked group, the group with CTC gives cavitation inception noticeably earlier. Additionally, CTC-spiked blood sample have also significant difference with N1 group.

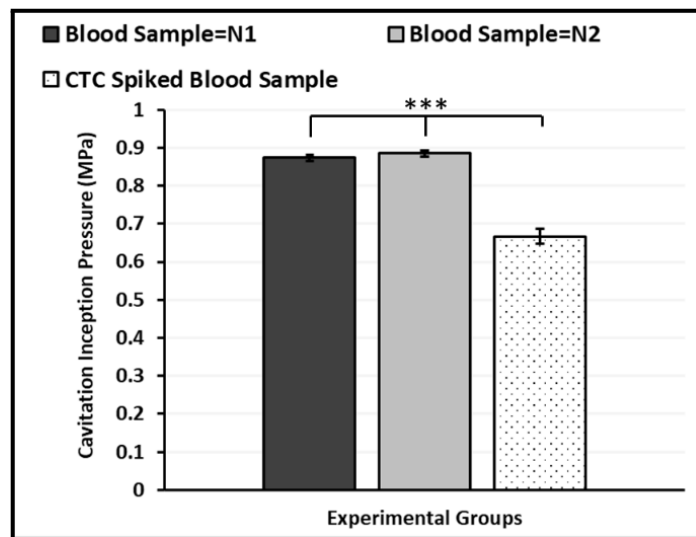


Figure 9: Column graph of the cavitation inception pressure of different blood samples. The blood sample (N1) and the blood sample (N2) represent the different collections of the blood samples from volunteers. The last group is a blood sample with CTC spiked into the N2 group.

2.4. Discussions

This study introduces a method, which enables rapid detection of the CTCs within minutes. Most of the CTCs have a very short survival time due to several reasons such as shear stress of flow, anoikis, and extravasation [61]. In circulation, limited half-life of CTCs is between 1-2.4 hours, which implies short time for detection [62]. The quick diagnosis capability of this method could detect the intravascular cancer cells before their disappearance time, unlike detection methods with specific labels that are more costly and demanding.

This research study utilizes cell culture tools and cancer cells-spiked blood during the initial investigation and development phase of CTC detection tool, which is crucial to understand the mechanism of the detection technology in early stages. On the other hand, the current study aims to detect whether there are CTCs in the blood of patients rather than collecting them for analysis purposes in the subsequent studies. The results show that the Jurkat+ CTC group possesses earlier cavitation inception than other groups by creating more heterogenic environment, which means cancer cells in the sample fluid can be detected by using the cavitation phenomenon on Chip-wo-R (Figure 5). Moreover, group CTC demonstrates more inception pressure reduction than group Jurkat since the CTC group provides a more noticeable size within the medium than the Jurkat group, which affects inception pressure as one of the main factors (Figure 5). Hence, rheological characteristics of a liquid alter when it includes cells with different sizes and characteristic properties. The MDA-MB-231 and Jurkat cell have different mechanical and biophysical characteristics [63,64]. Thus, the difference in cavitation inception upon micro-level changes within the medium could be utilized as a valuable marker of different rheological characteristics. The cells with different rheological and physical properties inside a liquid affect the cavitation inception behavior substantially, particularly when the cells have a surface area with a different magnitude, and the surface has nano/micro-level irregularities. Our results show that the cavitation bubbles' occurrence are dependent on the shape of the channel and the content of the working fluids. The reduction of inlet pressure required for the inception cavitation in presence of immersed particles and surface roughness could be explained based on the heterogenous nucleation theorem. Within a liquid, nucleation stems from the ephemeral microscopic voids created by random molecular motion inside the liquid paving the way

for the nuclei to grow and rupture. In heterogeneous nucleation, the voids are originated at the interface of the liquid/solid/vapor intersection of the suspended particles or channel wall. Therefore, the contact angle of the bubbles on the surface of the nucleation site plays an important role in the reducing the tensile strength of the liquid. This reduction in tensile strength at the boundaries of the channel wall and suspended particles turns them into the potential cavitation bubble nucleation sites, which are called ‘surface nuclei’ and ‘stream nuclei’, respectively. Thus, the stream nuclei originating from the particles-here the cells- and surface nuclei caused from the sidewall roughness elements are major locations of bubbles generation. This also causes the pressure reduction in the inception of the bubbles. Our results for using two sets of microfluidic devices with and without sidewall roughness elements showed that when the dominance of the stream nuclei is preserved with using smooth sidewalls, detection of CTCs from Jurkat cells was enhanced. A reason could be that by suppressing the surface nucleation sites, presence of CTCs as stream nucleation sites became the sole reason for tensile strength reduction in the liquid. According to cell size distribution graph (Figure 8), CTCs have a larger diameter. Thus, CTC-spiked mediums consequently have early cavitation inception (lower upstream pressure) compared to the Jurkat group without any CTCs. In the light of SEM analysis, the study identifies the difference between the morphological features of the cells, such as size, as the most significant parameter in obtaining a lower cavitation inception value in the group containing CTCs. Our subsequent research studies focus on determining the effects of properties such as stiffness of cells and working fluids. For this aim, the further studies will also evaluate the AFM force measurement analysis and discuss how cell elasticity could affect cavitation inception. The different morphological properties of cells contribute to the change in cavitation inception behavior without utilizing immunological profile of them. Hence, the HCOC captures CTCs without being affected by heterogeneous cell distribution resulting from the epithelial-mesenchymal transition. However, unlike some current technologies, the HCOC system does not offer isolation, enumeration, and retrieval of CTCs. Instead, it provides only the detection of very rare CTCs in biological fluids such as blood.

The HCOC system can detect the presence of CTC down to 50 CTCs/mL in the experiments carried out so far as an initial study (Figure 7). Even there is a six-fold difference between the concentrations of 300 CTCs/mL and 50 CTCs/mL, the

difference is only 250 CTCs/mL, which is extremely low compared to total cell (CTC+Jurkat) present in the system. This could be the reason that the difference between the experimental groups containing the lowest and highest CTC concentrations cannot be detected by HCOC. In contrast, the presence of the CTCs can be detected in both groups. In clinical approach, after the removal of red blood cells from blood, the ratio of CTCs and white blood cells should be considered. In the blood of a healthy person, there are 1-4 million lymphocytes [65,66], while in a patient, the number of CTCs can vary between 1-1000 per mL [5,6]. Therefore, the applicability of CTC concentration in the clinic is close to 1-1000 CTCs/ 1-4 million lymphocytes. Accordingly, the study used Jurkat cells and CTCs with the ratio is 50-300 CTCs/1 million Jurkat cells to mimic a mixture of mononuclear immune cells and CTCs. Even though the number of CTCs in the patient's blood is meager, some studies showed that there are 39 CTCs/2 mL in the nonmetastatic group and 119 CTCs/2 mL in the metastatic group [67]. The HCOC detection limit is 50 CTCs/mL in this study. This number is close to the number of CTCs in the metastatic group, which implies that the HCOC enables the detection of CTCs in the metastatic group in the range of 50-300 CTCs/mL. In order to increase detection sensitivity, configuration of devices such as hydraulic diameter, L/d ratio and surface or sidewall roughness properties should be further optimized. The cavitation inception results of different CTC concentrations affirm the reliance on a satisfactory level of CTC detection. In the blood, CTCs travel as single cells or in clusters by aggregation, and it was reported that CTC clusters had a higher potential for metastasis [68,69]. Since CTC clusters consist of aggregates of cells, they are expected to lead to lower cavitation inception and to facilitate to be detected in HCOC.

Each individual could have different concentrations of protein in blood [70]. Human blood is composed of cells, lipids, and proteins. Most of this composition is coming from cells, followed by proteins and lipids. The total protein content of a healthy person is 6-8.3 g/dL, whereas the total cholesterol is less than 200 mg/dL (0.2 g/dL). From a clinical biochemist point of view, fluctuations in blood protein levels are more relevant to affect blood viscosity and interfere with biochemical detection processes. Therefore, we performed real sample tests to observe cavitation inception within device working with blood sample from different volunteers. The results demonstrate that even healthy blood with different property bring about cavitation inception at approximately the same

pressure (N1, N2). Size of the molecules within blood such as proteins, lipids are in the nanoscale, which results in no effect in the process of cavitation inception in the proposed detection sensitivity. Moreover, the CTC-spiked blood sample has very significant difference compared to the same blood sample without CTC in terms of inception pressure. Here, CTC demonstrates a dominant effect against blood components comprising the largest component even smaller than CTC based on their sizes. Hence, the results proves that the HCOC system can detect CTC in real samples. It is noteworthy to mention that red blood cells elimination is generally required for CTC detection procedures. There are many technologies available for their separation including straightforward and conventional methods such as centrifugation along with cutting edge technologies [71]. The elimination of red blood cells results in a mixture of mononuclear immune cells and CTCs [72]. However, red blood cells could be separated by straightforward and conventional fashion such as centrifugation rather than sophisticated technologies. On the other hand, the amount of blood sample used for each experiment is 200 mL. Integration of a low-cost microphone capable of detecting the cavitation inception noise allows CTC detection even in tiny volumes, which is considered for a more sensitive system. Therefore, it is expected that more sensitive systems with lower volume could be obtained by a more sensitive detection system.

3. CHAPTER THREE: CANCER TREATMENT USING FACILE HYDRODYNAMIC ON A CASCADE DEVICE

3.1. Research Objectives

Hydrodynamic cavitation (HC) is a phase change phenomenon, where energy release in a fluid occurs upon the collapse of bubbles, which form due to the low local pressures. In recent years, due to advances in lab-on-a-chip technologies, HC-on-a-chip (HCOC) and its potential applications have attracted considerable interest. Microfluidic devices enable the performance of controlled experiments by enabling spatial control over the cavitation process and by precisely monitoring its evolution. In this study, we propose the adjunctive use of HC to induce distinct zones of cellular injury and enhance the anticancer efficacy of Doxorubicin (DOX). HC caused lysis, necrosis, permeabilization, and unaffected regions upon exposure of different cancer and normal cells to HC. Moreover, HC was also applied to the confluent cell monolayer following the DOX treatment. Here, it was shown that the combination of DOX and HC exhibited a more pronounced anticancer activity on cancer cells than DOX alone. The effect of HC on cell permeabilization was also proven by using carbon dots (CDs). Finally, the cell stiffness parameter, which was associated with cell proliferation, migration, and metastasis, was investigated with the use of cancer cells and normal cells under HC exposure. The HCOC offers the advantage of creating well-defined zones of bio responses upon HC exposure simultaneously within minutes, achieving cell lysis and molecular delivery through permeabilization by providing spatial control. In conclusion, HC proposed a promising alternative to be used to increase the therapeutic efficacy of anticancer drugs. Our approach has the potential to be easily integrated to clinical and *in vivo* studies, in the near future.

3.2. Experimental Method

3.2.1. Cell Culture

SH-SY5Y, MCF-7, HUVEC, A549, and Beas-2B cells were used in cell culture studies. SH-SY5Y, HUVEC, MCF-7 and A549 cells were cultured in DMEM-F/12 medium

containing 10% FBS, 1% penicillin-streptomycin, while Beas-2B cells were cultured in DMEM. Cells were incubated at 37°C in a humidified incubator containing 5% CO₂. After the cells became confluent, they were washed with PBS and then trypsinized. Cells were centrifuged at 2000 rpm for 5 minutes and supernatant was discarded. Cell counting was performed using the Thoma chamber after trypan-blue staining, and cells were seeded with the density of 100 x 10³ cells on PMMA (poly-methyl methacrylate) surfaces (1 cm x 2 cm), which were sterilized previously, and cell culture well plates.

3.2.2. Hydrodynamic Cavitation Treatment

After the cells became confluent on the PMMA surfaces, cavitation tests were performed. To prevent possible catastrophic effects of HC on cells, the applied inlet pressure was chosen to be 758 kPa, which corresponded the HC inception pressure in the microfluidic device.

3.2.3. Microfluidic Device Design, Fabrication and Experimental Procedure

3.2.3.1. Fabrication Method and Device Configuration

The utilized microfluidic device contains one inlet and eight parallel micro-orifices with an open wall as the outlet, where the fluid stream exits the device. Each micro-orifice consists of lateral wall structured roughness elements to facilitate cavitating flow formation. The schematic of the implanted device is displayed in Figure 1, and the important dimensions are included in Table 1. The implemented micro-fabrication techniques were given in detail in the previous study of Shafaghi *et. al.* [73]. Considering that the microfluidic device is at pressures lower than 758 kPa, the packaging unit of this device could allow visualization for inspection. A similar package was also used in the previous study of Shafaghi *et. al.* [73]. The cavitating flow patterns were recorded using the Phantom VEO-710L high speed camera. The performed visualization was based on the shadow graph technique using a light source, which illuminated on the silicon surface. A K2 DistaMax macro camera lens was employed to magnify cavitating streams inside microchannels of the microfluidic device. Figure 10 summarizes experimental procedures of the study before and after HC.

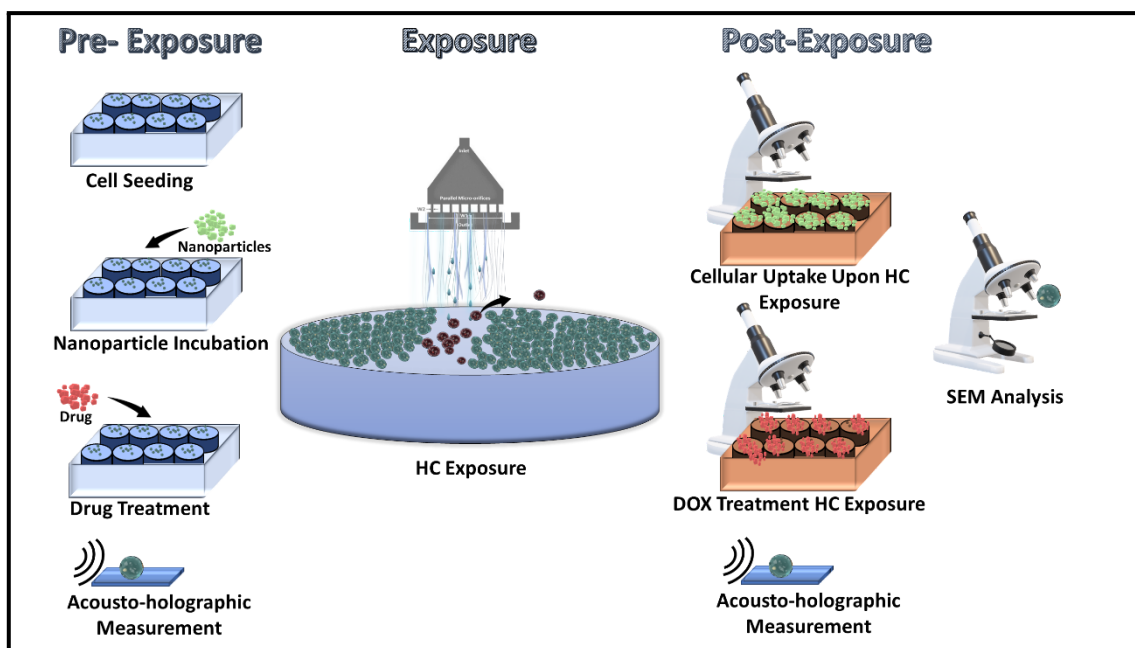


Figure 10: Schematic summary of experimental procedures before and after hydrodynamic cavitation exposure.

3.2.4. Determination of Cell Proliferation Under DOX Treatment and Hydrodynamic Cavitation

Cytotoxicity analysis was performed to investigate the effect of HC alone and in combination with DOX treatment on the proliferation of normal and cancer cells. The cells were first seeded into 6 well plates with the density of 0.3×10^6 cells per well and were incubated overnight. Then, the cells were treated overnight with DOX at concentrations of 0.5 mM, 1 mM, and 2 mM, respectively. Then, the cells in the well plates were exposed to HC at an inlet pressure of 758 kPa. To prevent any possible catastrophic effect of HC on cells, the inlet pressure was chosen to be 758 kPa, which corresponds to cavitation inception. Finally, all liquid covering the cell layer was discarded, and the MTS solution was added so that cell viability could be determined. After the cells were incubated with MTS for 4 hours, the absorbance values were measured at the wavelength of 490 nm. As a result, with DOX only, HC only, and both DOX +HC were evaluated on all cell lines. The concentration profiles as a function of the cell viability were obtained for each cell line, and the results were evaluated by comparing them with each other.

3.2.5. Morphological Analysis of Cells Upon Hydrodynamic Cavitation

SEM (Zeiss Leo Supra 35 VP, Germany) analysis was performed to examine the morphology of the cells upon HC exposure and to perform a detailed morphological analysis of the effects on different cell lines. First, the cells were seeded on a PMMA surface and fixed on the surface after being exposed to HC. The fixation step was carried out by incubating the cells with a 2.5% glutaraldehyde (FLUKA, 49629-1L) solution in 0.1M PBS for 2 hours. Then, dehydration was carried out with washing in an ethanol series containing 35%, 50%, 70%, 80%, 90%, 95% and 100% ethanol for 10 minutes, respectively. HMDS (Hexamethyldisilazane) (Thermo Fisher Scientific, AC120580100) was introduced to cells with gradients of 50%, 60%, 70%, 80%, 90% and 100%. The samples, which were then left to dry at room temperature, were vacuumed for 15 minutes and coated with gold-palladium for 5 minutes. SEM analysis was performed at an acceleration voltage of 2 kV.

3.2.6. Calcein AM/PI Staining for Live/Dead Cell Imaging

Calcein AM/PI staining was performed to analyze the dead/living cells formed in the cavitation zone. This method was based on the combination of Calcein AM, which could be hydrolyzed by living cells, and PI, which was permeable only to dead cells. In the experimental stage, 1 mM Calcein AM stock solution was prepared in DMSO (1 mg/mL). Then, the stock was diluted in PBS (20 μ m/10 mL), resulting in 2 μ M Calcein AM. The prepared solution was used to treat cells for 1 hour. Then, the PI working solution was prepared with a concentration of 5 μ g/mL by diluting the 1 mg/mL stock solution in PBS. Then, the cells were treated with this PI solution for 1 hour [74]. After incubation, all the liquid was removed from the cells, and analysis was carried out by means of a fluorescent microscope (Carl-Zeiss Live Cell Imaging Microscope Axio Observer. Z1).

3.2.7. Detection of Enhanced Cell Permeability by CDs

To show that the cell permeability and cellular uptake can be increased with the help of HC. The cationic aqueous carbon dot “AFF0₃”, which has emission peak at 515 nm and

size between 109-154 nm, synthesized by Ahmet Ferid Firat and Prof. Havva Yağcı Acar. CDs were diluted in PBS with the ratio of 1:10 from the stock solution and were examined via a fluorescent microscope after 10 min treatment with cells upon HC exposure. In addition, the confluent cells were incubated 10 mins, 30 mins, 1h and 3h with 1:10 dilution ratio of CDs in PBS to observed cellular uptake without HC exposure.

3.2.8. Production of PZT Transducer-Embedded Microfluidic Chambers

The PDMS fluidic chamber was produced by the soft lithography technique. Firstly, pre-polymer and curing agent were mixed at a 10:1 (w/w) ratio. The mixture was degassed for 30 min in a desiccator to remove any air bubbles from the polymer. Then, the polymer was poured into a mold, and a PZT transducer was placed on the polymer. The final structure was baked at 60°C for 3 hours, and a partition with the dimensions of 12 mm x 12 mm x 5 mm was cut and then peeled off from the mold. The oxygen plasma application at 400 mTorr pressure and high power of 2 minutes were applied for irreversible bonding of PDMS structure and glass slide.

3.2.9. Optic Measurement of Cell Stiffness by Acousto-Holographic

After HC exposure with 758 kPa upstream pressure of cell monolayers, the acousto-holographic microscope was used to examine the effects of changes in the membrane structures of cells by using the methodology stated in the study of Varol et al. [75], which reflects the biomechanical properties of these cells. This method does not require any marker molecule, is free from probe-cell interactions, and allows the cells to be examined in the medium. For this, the cells were first seeded at a density of 5×10^3 cells in microfluidic chambers. After the cells were adhered to the surface, they were stimulated by bulk acoustic waves generated by the PZT transducer at a frequency of 10 Hz. The acoustic pressure of the bulk acoustic waves induced a periodic compression and expansion over the cell membrane. The mechanical response of the cell was then measured using a phase-shifting inline Mach-Zehnder interferometer and a high-speed CMOS (complementary metal-oxide-semiconductor) camera. The displacement distribution (the difference between the thickness value measured at a given time

compared to the initial thickness value for a given point on the cell surface) was then extracted as a function of time. By means of this displacement parameter in the membrane, the elasticity modulus of the cells was calculated, and the cell stiffness information was obtained [75].

3.2.10. Statistical Analysis

All experiments were conducted at least in triplicate. The mean values, standard deviations and standard error values of all obtained results were reported. Relationships among groups were analyzed using one-way ANOVA (SPSS 12.0, SPSS GmbH, Germany), [Newman–Keuls multiple comparison test (* $p < 0.05$, ** $p < 0.01$, *** $p < 0.001$)].

3.3. Results

Confluent cell monolayers were exposed to cavitation flows generated inside eight parallel micro-orifices. First, cavitating flow patterns are visualized to assess the cyclic effect of cavitation and flow physics on cellular response. Then, different zones of cellular response on a plate created by HCOC were characterized. According to the results, HCOC leads to different cellular response zones: cell lysis, cell necrosis, cell permeabilization, and no-response region (Figure 11). The cell lysis region was analyzed by SEM to observe the impact of the bubbles on cells. Viability assays were performed to evaluate the viability of the cells adjacent to the lysis region, which allowed distinguishing between the necrosis and permeabilization region. Cellular uptake tests were carried out with and without HC-exposed groups to ensure the effect of HC on permeabilization. Following the investigation of permeabilization and cellular uptake, HC-enhanced drug treatment was reported based on cell viability. Finally, biomechanical properties of cells were investigated, which enabled the interpretation of the effect of the cell stiffness on cell permeabilization and lysis efficiency.

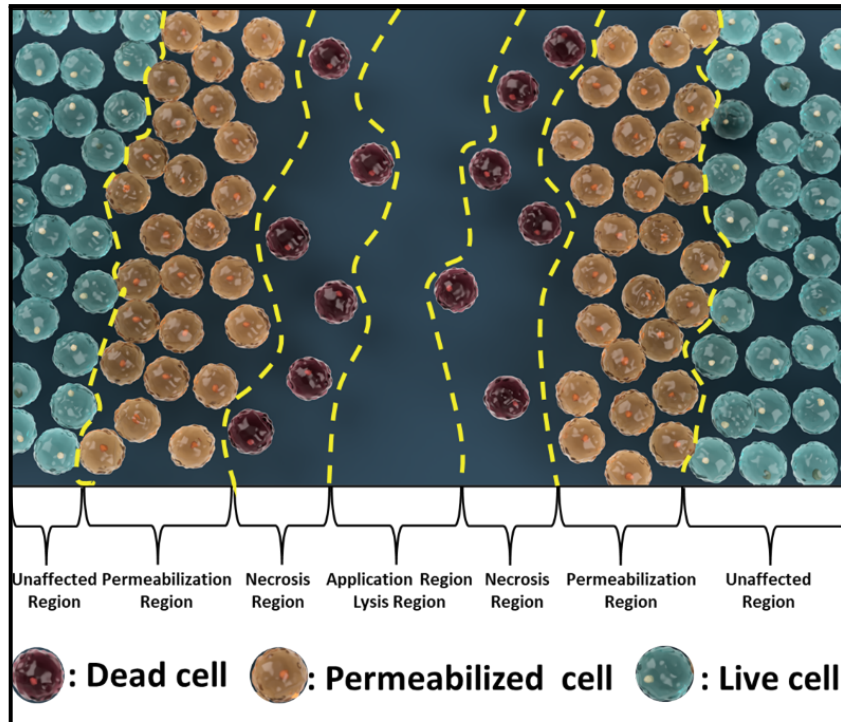


Figure 11: Illustration of zones of cellular effect created by HC.

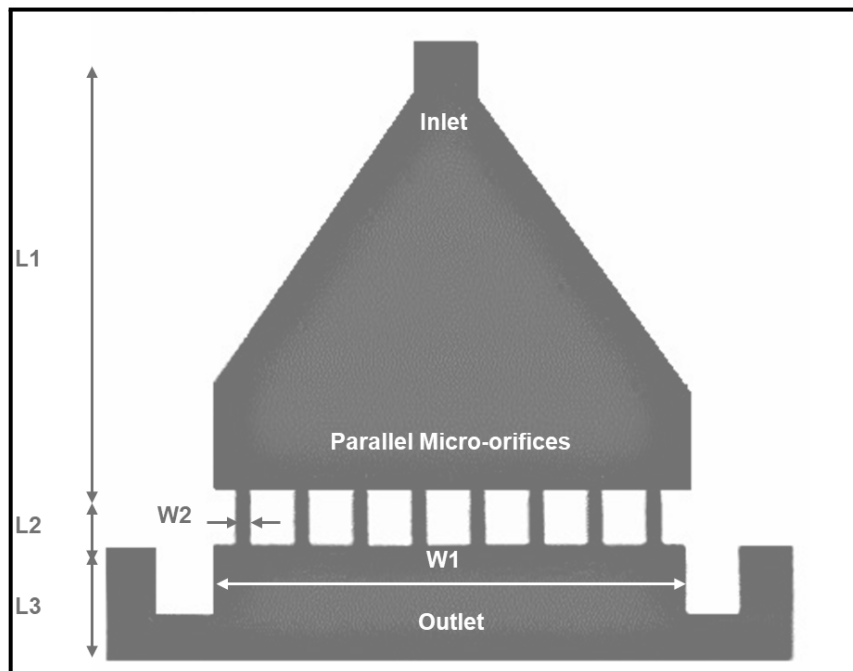


Figure 12: Microfluidic device configuration. Inlet Region Length (L_1) is 2000 μm , Micro-orifice Length (L_2) is 1000 μm , Outlet Region Length (L_3) is 2000 μm , Outlet Region Width (W_1) is 7800 μm , Micro-orifice Width (W_2) is 300 μm .

3.3.1. Characterization of the Zones of Cellular Response

The cavitating flow reaches to the center of the petri dish covered with a confluent cell monolayer and creates a roughly rectangular region due to the parallel arrangement of cascade multi-channels. According to the cellular response to HCOC cavitation, four separate regions exist. Upon HC exposure, a phase contrast image was taken under the fluorescent microscope. The phase contrast image (Figure 12) demonstrates that the cells were lysed, detached, and washed due to HC in the region, where the cavitation flow directly touches the petri dish. In contrast, nearby cells (separated from the middle region by the yellow line) were positioned apart from the cavitation application region and remained attached to the surface.

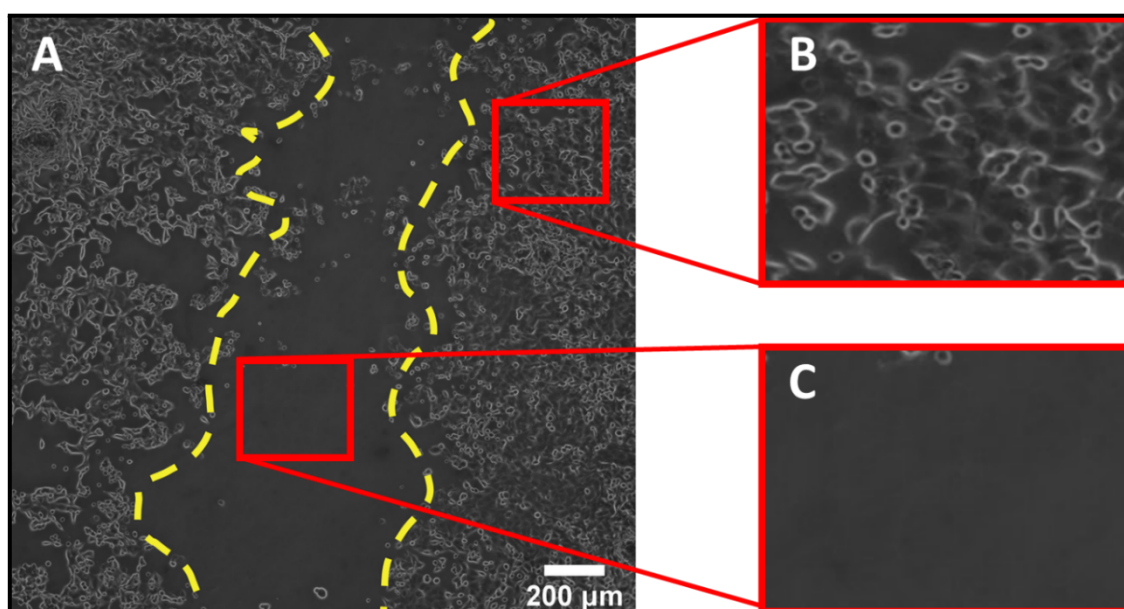


Figure 13: **A)** Phase-contrast image of Beas-2B cells upon HC exposure. HC exposure results in detachment of the cells from the exposure area. The cells adjacent to the exposure region are still attached to the surface. The yellow line separates the different regions based on cellular response. **B)** zoom-in image of the region of attached cells and **C)** zoom- in image of the detached cells from the surface.

The following section presents the effect of HC on cells and cellular membranes for a detailed analysis of the lysis region. The morphological changes of the cells were

affirmed by SEM images taken after HC exposure.

3.3.2. Characterization of The Morphological Changes After HC Exposure

Following the HC exposure through the center of the surface, the cells in the middle were affected more, and they were detached from the surface by the washing effect of HC. Hence, the detached cells were collected for further investigation and observation of the direct effect of HC on the cellular membrane and cell morphology. The detached cells were analyzed under the SEM microscope. Figure 13 demonstrates the SEM images of A549, Beas-2B, SHSY-5Y, and HUVEC cell lines subjected to HC. As can be clearly seen, HC bubbles rupture the cell membrane.

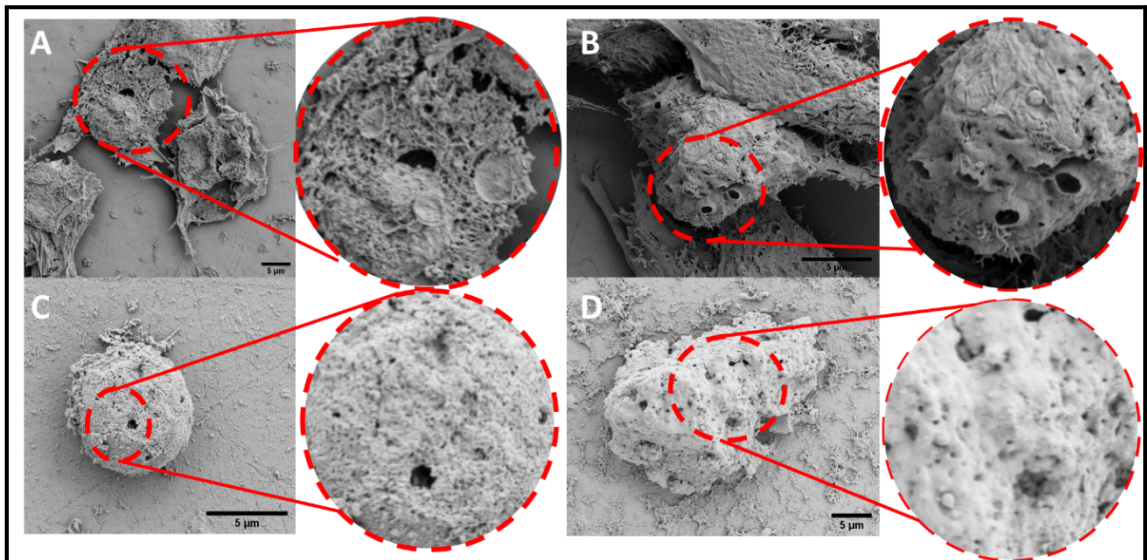


Figure 14: Detailed morphological SEM images of the lysed **A)** A549 cell, **B)** SHSY-5Y cell, **C)** Beas-2B cell **D)** HUVEC cell in the HC exposure area (lysis region). Cavitation bubbles damage the cell membrane due to imposing upon direct HC exposure, and different sizes of the pores are shown in the images indicated by red circles.

Following the analysis of the detached cells, a more in-depth investigation of the remaining attached cells was provided in the following section. Live and dead assays were performed to observe whether the attached cells were alive or dead.

3.3.3. Fluorescent Examination of Live/Dead Cells by Calcein AM/PI Staining

After cell lines were exposed to HC, a standard live and dead assay was performed for the purpose of distinguishing different cell responses. Accordingly, Figure 14 demonstrates fluorescence images of adherent Beas-2B and A549 cells following viability staining for regions affected by HC. Beyond this region, a necrotic cell is revealed in red under the microscope after performing the viability assay. It remains attached to the surface but is not alive. Nevertheless, the high percentage of viable cells maintains their attachment, which is apparent in green under the microscope. Besides, Beas-2B and A549 cell lines exhibit different responses upon HC exposure as shown in Figure 14. The corresponding detachment area of each cell line was calculated by the ImageJ program. Accordingly, the area of the detached A549 cells is 25.26 mm^2 while the dark region on the surface is 3.337 mm^2 for Beas-2B.

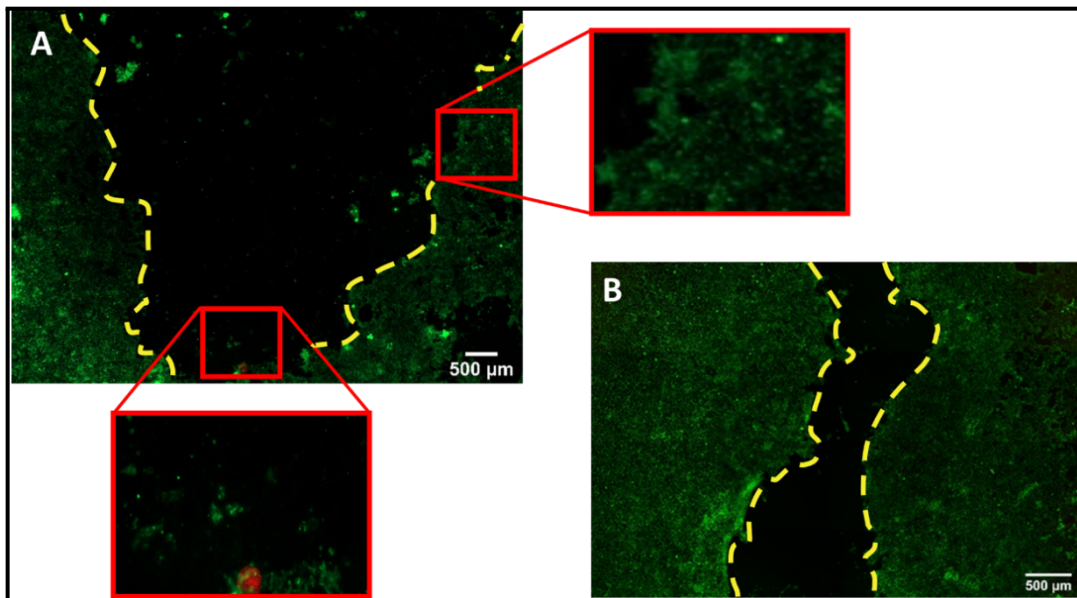


Figure 15: Fluorescent images of the **A)** A549 cells and **B)** Beas-2B cells after Calcein AM-PI staining following HC exposure. The different regions appear based on cell attachment upon HC exposure. Most of the detached cells are washed with the help of HC. Some cells keep their attachment, but not their viability. The green color represents the viable cells, while the red color refers to dead cells.

Following Calcein AM-PI staining, which demonstrated the live and dead cell regions, further investigation was required to observe the effect of HC on live cells. For this reason, cellular uptake tests were performed with/without HC exposure. The following

section reports the results on CDs uptake of cells with/without HC exposure.

3.3.4. Demonstration of Cellular Uptake Upon HC Exposure

Since a high percentage of attached cells maintain their viability upon HC exposure, there could be a distinct cellular response of cells against cavitation application regarding their distance from the direct application region. Hence, we investigated the impact of the HC on the cell membrane as well as the potential for cellular uptake. For this reason, the cells were exposed to carbon dot (CDs) nanoparticles, emitting green light, following the cavitation exposure. Figure 15 combines a bright-field image of cells and a fluorescent image of CDs uptaken by the cells. As shown in the Figure 15, cells subjected to cavitation enable the uptake of CDs in the near region of the application area after 10 min. However, the uptake of CDs decreases when the distance increases from the HC application area and thus the intensity of green light also decreases.

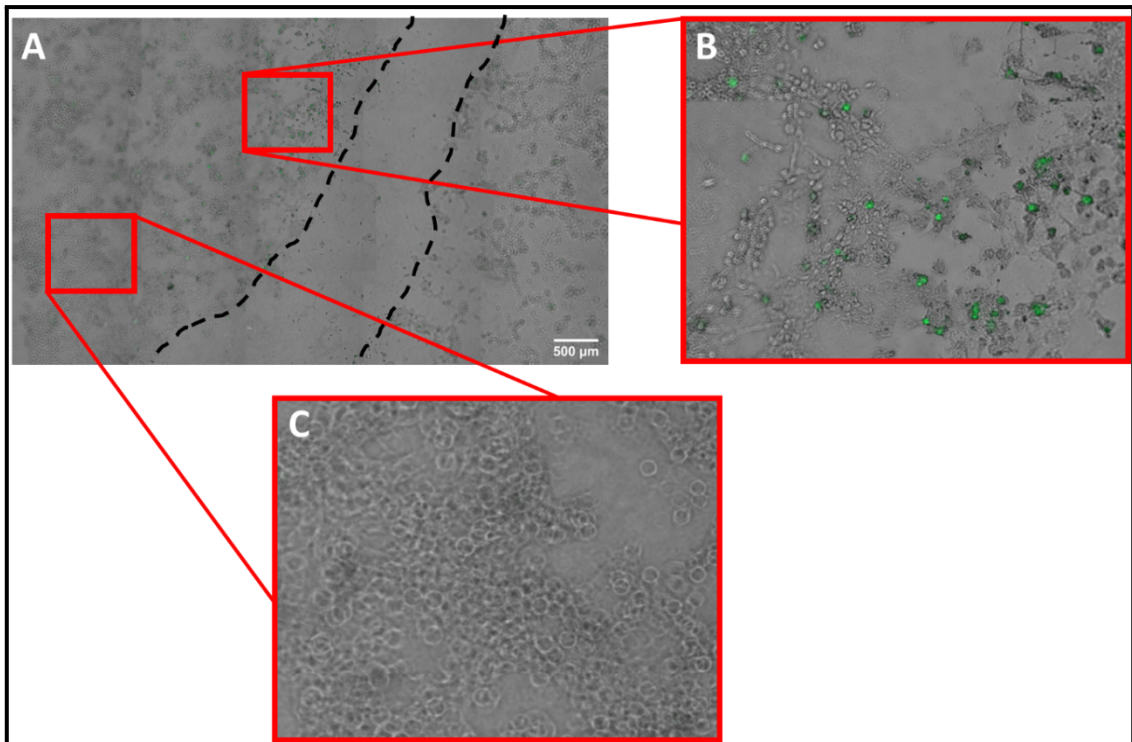


Figure 16: A) The combined fluorescent and bright-field images of the Beas-2B cells. B) Green color indicates the CDs uptaken by the cells closer to the HC application region. C) The image shows that the cells could not achieve cellular uptake due to the

large distance from the HC application area.

As a control group of CDs uptake, Beas-2B cells were seeded on well plates. After cells reached confluency, the cells were incubated with CDs for 10 min, 30 min, 1 h and 3 h, respectively (without HC exposure). In Figure 16, combined fluorescent and bright-field images demonstrate that the cells do not uptake CDs within the first 1 h. The uptake of CDs commences only after 3 h when HC is not applied. The green color in Figure 16 represents CDs inside the cells.

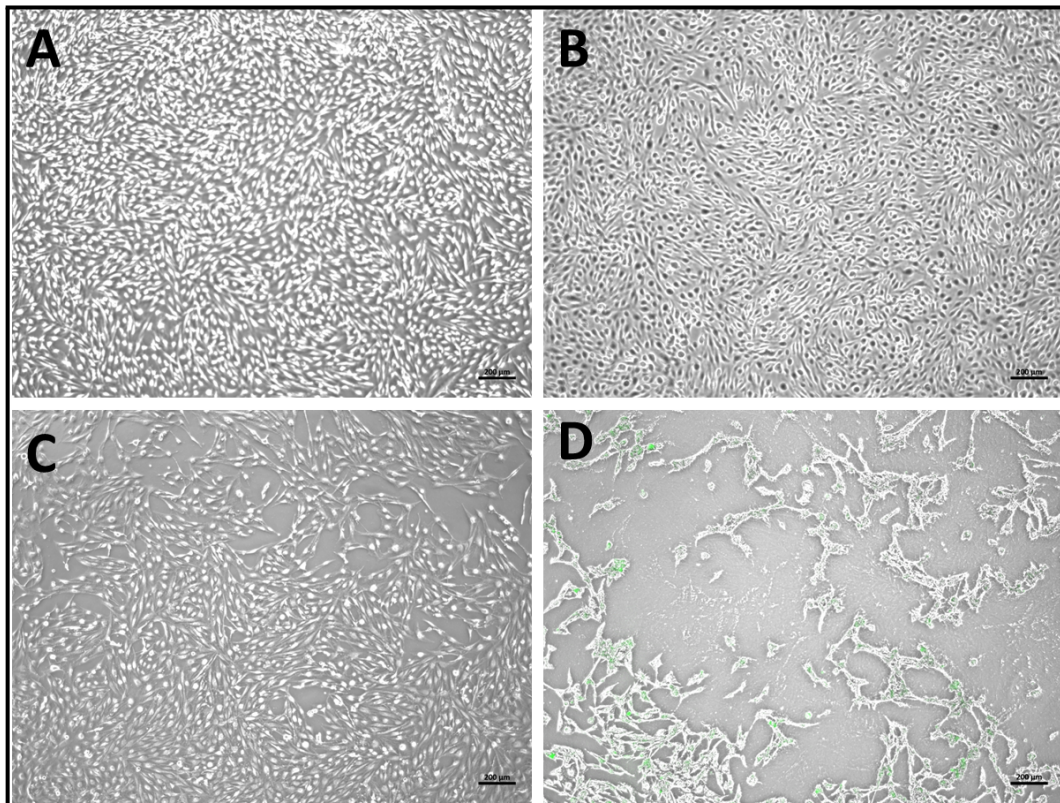


Figure 17: The combined fluorescent and bright-field images of the Beas-2B cells introduced CDs at different time periods. The cells introduced to CDs for **A)** 10 min, **B)** 30 min, **C)** 1 h and **D)** 3 h without HC exposure. Green color indicates CDs uptaken by the cells.

CDs cellular uptake demonstrates that HC can permeabilize cellular membrane and thus facilitate the uptake of CDs. After ensuring that the uptake of CDs is enhanced upon HC exposure, we investigated the DOX effect on cancer and normal cells. In the next section, related results are presented.

3.3.5. Changes in Cell Viability After HC + DOX Treatment

After confirming that cellular uptake can be increased in the area adjacent to the cavitation region, the effect of HC on the efficacy of drugs used in cancer treatment was investigated. Consequently, there are three different groups of each cell line, for which MTS cell viability assays were performed to assess the HC effect on viability and drug treatment. These groups are the (1) control group without any treatment or application, (2) only the DOX-treated group, (3) the HC exposed group, and (4) the HC-exposed group following with DOX treatment.

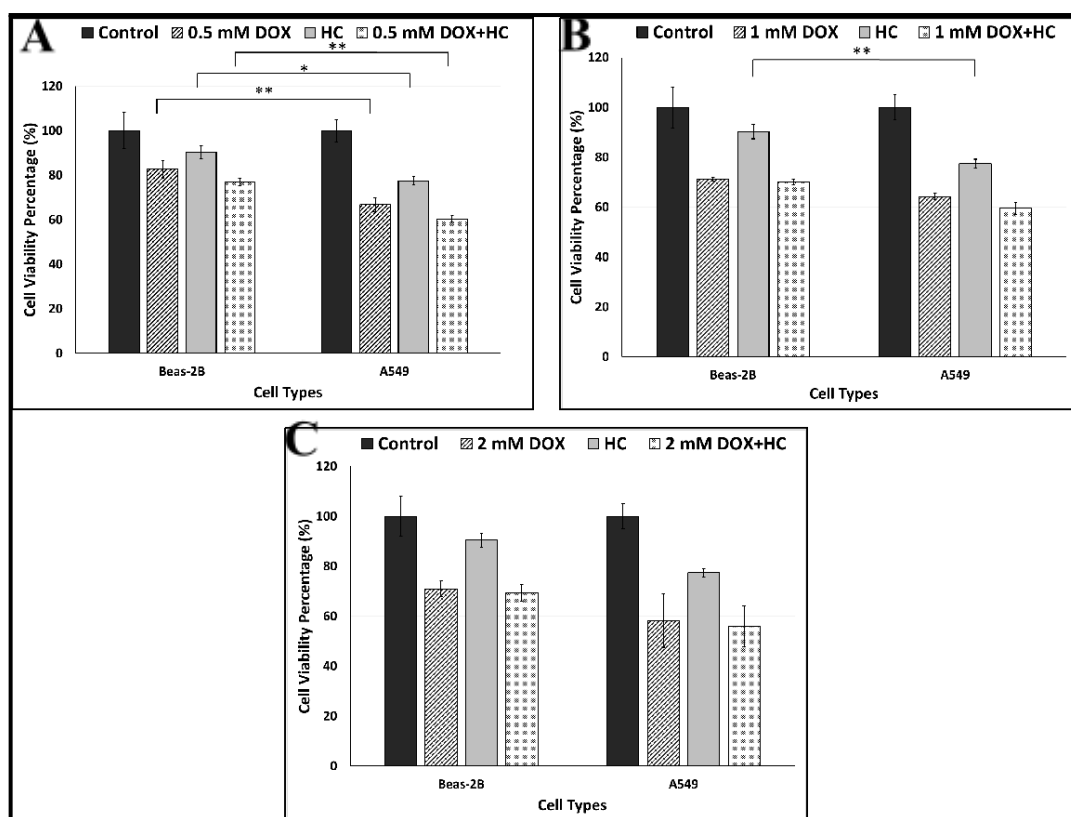


Figure 18: Cell viability profiles of Beas-2B and A549 cells. Cell viability is shown for cases without any treatment and exposure (control), with treatment different concentrations of DOX. [A) 0.5 mM, B) 1 mM, C) 2 mM], upon HC exposure and after different concentration of DOX combination with HC exposure.

To analyze the effect of HC on normal and cancer cells, Beas-2B (non-tumorigenic lung epithelial cell line) and A549 (lung carcinoma epithelial cells) cell lines, which belong to the epithelial cells, were used. The results shown in Figure 17 indicate that the

viability of 0.5 mM DOX-treated Beas-2B cell line is $82.66\% \pm 3.83$, while the HC exposed Beas-2B cells viability is $90.39\% \pm 2.93$, which proves that HC does not affect the cells more than DOX. Similarly, in A549 cells, cell death is less in the only HC-exposed group than in all the DOX-treated groups. The most remarkable result is that the HC-enhanced DOX treatment leads to more decrease in cell viability of cancer cells compared to normal (non-cancerous) cells at low concentration of DOX. For instance, only 0.5 mM DOX treated Beas-2B leads to $17.34\% \pm 3.83$ dead cells, while only 0.5 mM DOX treated A549 results in $33.24\% \pm 3$ dead cells. The difference between Beas-2B and A549 cells under DOX treatment with 0.5 mM + HC is significant. HC causes more cell death in cancer cells compared to normal cells at low concentrations. When HC is used together with DOX, a more pronounced anticancer activity emerges. After 2 mM DOX treatment, the percentage of the dead cells becomes $41.71\% \pm 10.73$ for A549 cells, and this value is $29.07\% \pm 3.20$ for Beas-2b cells. Besides, the percentage of dead cells becomes $44.12\% \pm 8.22$ of the HC-enhanced 2 mM DOX-treated A549 cells, while Beas-2B cells led to $30.73\% \pm 3.24$ cell death in the HC enhanced- 2mM DOX treatment. The results suggest that the difference between the normal and cancerous cells under DOX treatment with 1 mM + HC and DOX treatment with 2 mM + HC appears to be insignificant probably due to the saturated concentration of DOX.

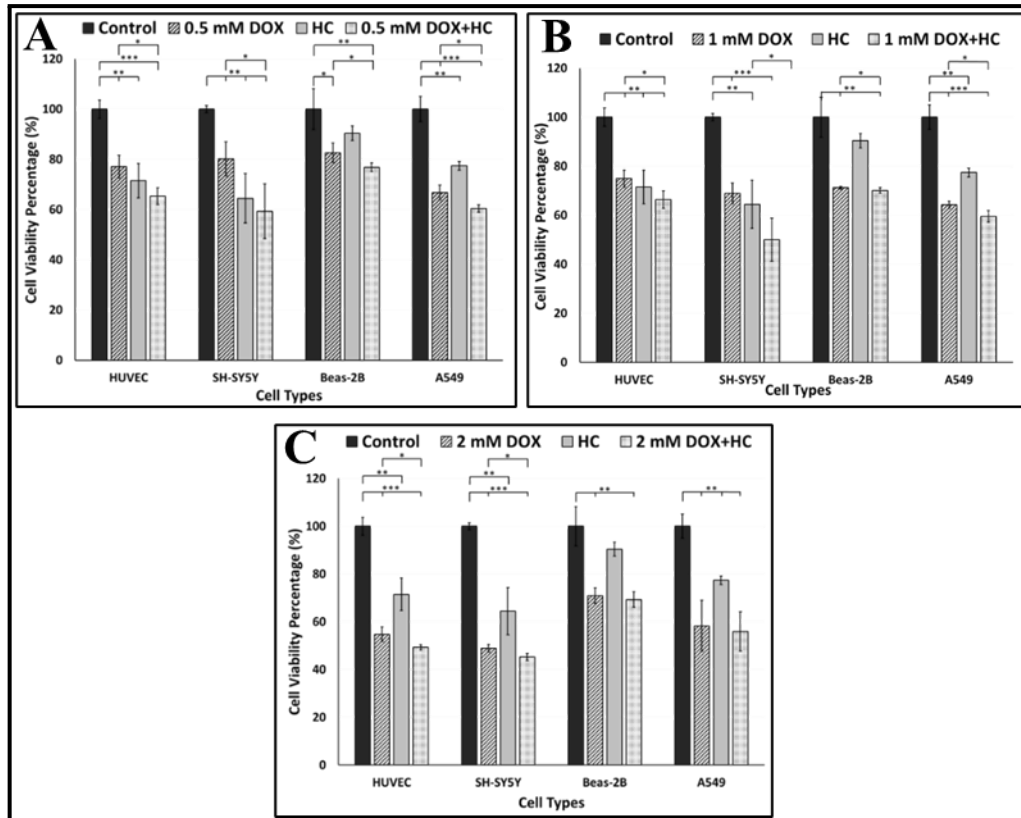


Figure 19: Cell viability profiles of HUVEC, SH-SY5Y, Beas-2B and A549 cells. Cell viability is shown for cases without any treatment and exposure (control), with treatment different concentrations of DOX. [A) 0.5 mM, B) 1 mM, C) 2 mM], upon HC exposure and after different concentration of DOX [A) 0.5 mM, B) 1 mM, C) 2 mM] combination with HC exposure.

Figure 18 shows the responses of different cell types to HC-enhanced DOX treatment. As normal (non-cancerous) cell lines, Beas-2B and HUVEC cell lines were used for the comparison of the results with cancer cell lines. Although all cancer cell types and normal cell types react differently, the HC-enhanced DOX treatment mostly results in more cell death in cancerous cells than normal cells. According to the results shown in Figure 18, the control groups are assumed to have 100% cell viability since there is no cavitation application or treatment. DOX concentration and cell toxicity have a direct relationship, which agrees with the findings in the literature [76,77]. Therefore, an increase in DOX concentration leads to a decrease in cell viability for both normal (non-cancerous) and cancer cells. The cell viability percentage of HUVEC cell line treated with 0.5 mM DOX is $77.05\% \pm 4.53$, while it is $54.77\% \pm 3.00$ for 2 mM DOX.

Moreover, HC reduces the cell viability less than DOX treatment for almost all the groups. According to the results, the viability under the only DOX treatment is $77.05\% \pm 4.53$ for HUVEC cells, while the HC-enhanced DOX treatment leads to $65.38\% \pm 3.35$ cell viability for HUVEC. Similarly, the viability of SHSY-5Y is $80.22\% \pm 6.79$ for the only DOX case. However, the HC-enhanced DOX treatment results in $59.34\% \pm 10.95$ cell viability. The same trend is observed for 1mM DOX treatment. Accordingly, the HUVEC viability is $74.92\% \pm 3.48$ under only DOX treatment, while this value changes to $66.44\% \pm 3.55$ for the combination with HC. Likewise, SHSY-5Y cells have $68.88\% \pm 4.26$ cell viability under DOX treatment and $50.04\% \pm 8.82$ cell viability under the HC-enhanced DOX treatment, respectively.

According to the results, different cell types have diverse deformation modes upon HC exposure in the lysis region (Figure 13). Furthermore, the cells react dissimilarly to DOX treatment and HC exposure, as shown in Figure 17 and 18. The reason behind this is linked with different mechanical characteristics, which could affect lysis and permeabilization efficiency due to varying cell stiffness values. Therefore, the biomechanical characterization of the cells is included in the next section.

3.3.6. Effect of The HC on Biomechanical Properties of The Cells

The effect of the HC with upstream pressure 758 kPa on cell biomechanics was investigated for A549 and BEAS-2B cells. Figure 19 presents the results of the acousto-holographic microscopy, which shows the maps of the cell's stiffness. The average stiffness values derived from these maps are 3.44 kPa, 3.08 kPa, and 3.21 kPa, for three different A549 cells, measured as control. After being exposed to HC, the stiffness values change to 2.40 kPa, 2.11 kPa, and 1.92 kPa for three different cells. On the other hand, the stiffness values of the control BEAS-2B cells are 2.58 kPa, 2.67 kPa, and 2.46 kPa. Upon HC exposure, these values change to 1.68 kPa, 1.92 kPa, and 1.48 kPa.

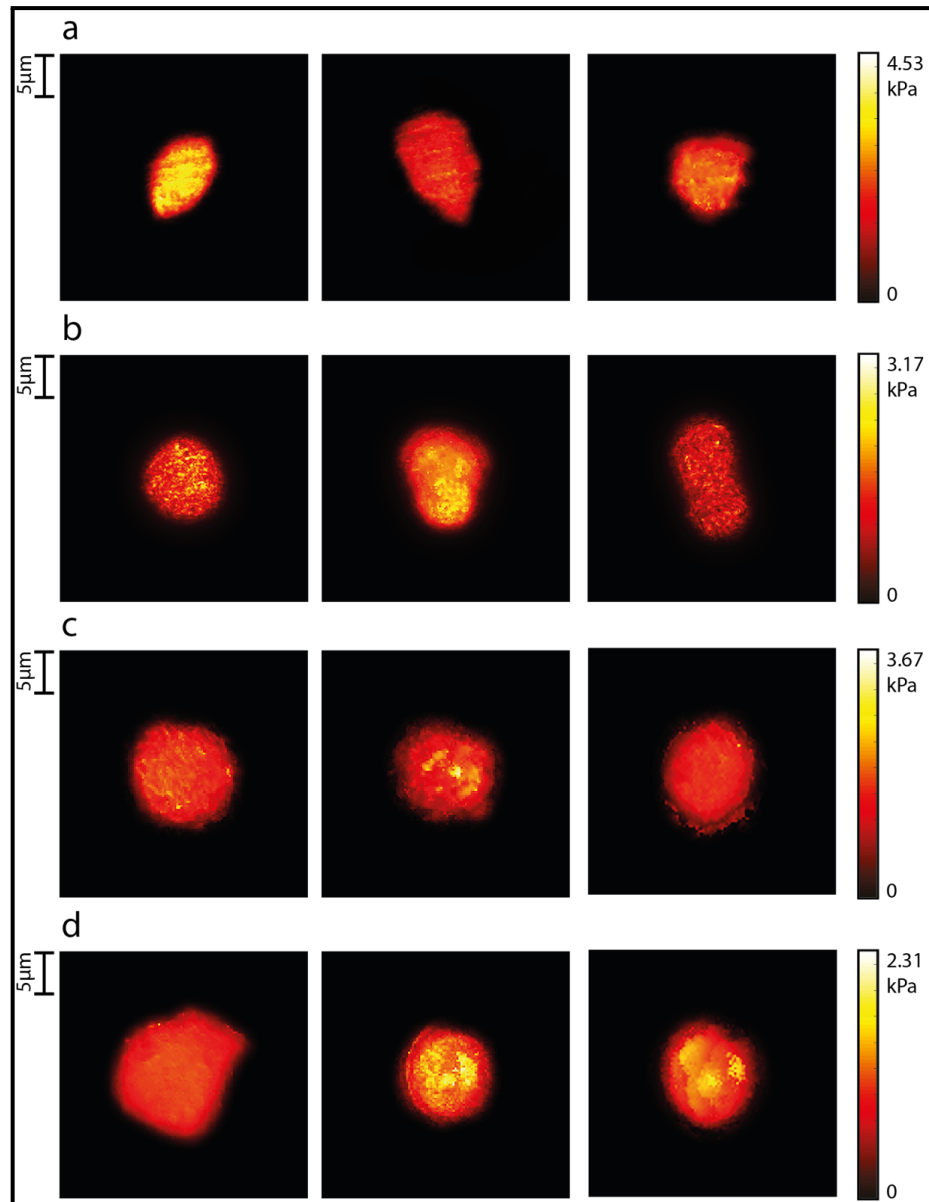


Figure 20: Acousto-holographic stiffness distribution of **(a)** A549 control cells, **(b)** BEAS-2B control cells, **(c)** HC-exposed A549 cells, and **(d)** HC-exposed BEAS-2B cells.

The results show that the stiffness values of both A549 and BEAS-2B cells decrease upon HC exposure. This can be explained by the fact that HC causes depolymerization of the cytoskeleton due to the pores formed on the cell membrane surface.

3.4. Discussions

The findings that we obtained indicate that there is a connection between the physics of micro-scale HC and the biomechanical response of the cellular entities. The concept of the HCOC enables to provide a manipulated biophysical response by allowing for spatial control. The tested device houses eight parallel structured microorifices. The HCOC device enables the formation of diverse cavitating flows at the same time while maintaining a constant upstream pressure. Moreover, the structured eight channels facilitate the initiation of the HC by decreasing the required input energy [78]. The HCOC device is advantageous in terms of its high efficiency compared to ultrasonic cavitation, which requires high power [79]. Besides, obtaining cell disruption or lysis is very rapid in HC compared to other cavitation techniques. For instance, Lee et al. [80] reported that sonication required 10 hours to achieve cell disruption while the operation time was 4 minutes for HC. Similarly, the HCOC allows the cell lysis process in only for minutes.

The HCOC device can create different regions of examination with high efficiency according to the distance from the application site. In the experiments, cavitation occurs inside the HCOC device, and the working fluid with atomized droplets travels through eight microorifices and bombards the cell monolayers, which are placed in front of the emerging jet streams. Due to the shear stress resulting from the cavitating flow, the cells react in different modes with respect to their location and cavitation exposure area. Mechanical lysis is a common method for physically disrupting the cell membrane due to its high lysing efficiency [21]. The HCOC device provides adequate energy and causes mechanical lysis in the direct application region (Figure 12). Since more energy is channeled to the application area, HCOC leads to more damage in this region. HC causes the cell structure to be destroyed in the exposed zone by rupturing cells and membranes, which ultimately results in the cell's contents exploding (Figure 13). The LINC complex (Linker of Nucleoskeleton to the Cytoskeleton) binds cytoskeleton components including actin microfilaments, microtubules, and intermediate filaments to nuclear membrane proteins [81,82]. This connection forms a physical contact between the nucleoskeleton and the cell cortex, allowing mechanical information from the surface of the cell to be transmitted through the cytoplasm [83]. Therefore, any mechanical impact on the cell membrane disrupts the membrane, which is rapidly conveyed to the cytoplasm. The mechanical effect due to HC exposure is transmitted

along the membrane-nucleus pathway, causing membrane rupture and fragmentation of the cell's organelles. The disrupted membrane allows cytoplasmic substances to leak outside the cell. The SEM images of captured single normal cells and cancer cells, which are exposed to cavitation, demonstrate the erosion of cytoplasmic contents. HC could therefore be used to create single-cell deformation and analysis (Figure 13).

The confirmation of the viability of cells adjacent to the HC exposure area indicates that HCOC creates a necrosis region by allowing less access to cavitating flow, where rare cells remain attached to the surface but are not alive (Figure 14). However, the regional surface areas of detached cancer and normal cells are different, which could depend on the characteristics of different cell types since cancer and normal cells have variable tolerance levels to physical stress [24]. In a related study, Kosheleva *et al.* [84] reported that A549 cancer cells were more sensitive to any damage by acoustic cavitation compared to Beas-2B cells. This finding is in agreement with our experimental results, and can be seen in Figure 14, more A549 cells rupture and are detached from the surface than Beas-2B cells according to surface area investigation, since the rupture tension is dependent on the differences in cytoskeletal characteristics between cell types, especially cancerous and normal cells. Furthermore, Figure 14 suggests that HC keeps the cells alive nearby HC exposure area. After detailed investigation on how live cells react against cavitation, this study proves that HC can permeabilize the membrane by cellular uptake test with and without HC exposure. Due to the sophisticated dynamics in cell-bubble interactions, the principle behind the permeabilization mechanism by HC has not been understood. The cytoskeleton network consists of hollow and long cylindrical microtubules, which comprise polymerized α - and β -tubulin dimers [85–88]. Hence, the stability of the microtubule cytoskeleton could be impaired by HC, resulting in the breakdown of the α -tubulin network. Also, the rapid weakening of cell-cell adhesion could assist the cell permeabilization through cavitation application. The membrane permeabilization process could give a more accurate representation in HC-enhanced drug delivery applications, where larger distances are employed to prevent unenviable cellular destruction. This could also be advantageous for HC permeabilization cases involving controlled bubbles, which could be connected to the cell membrane via ligand-receptor binding. Therefore, the results shown in Figure 15 prove the ability of HC in changing permeability and indicate that Beas-2B cells

cannot uptake the CDs within 3 hours without HC application, while the HC-exposed cells achieve cellular uptake within 10 min.

Furthermore, the ability in changing permeability with HC can be seen in the HC-enhanced DOX treatment for both normal and cancer cells. Compared to normal and cancer cells (Figure 17), HC-enhanced DOX treatment is more efficient on cancer cells at low concentrations. In conclusion, this approach offers a novel strategy for cancer treatment, with the additional benefit of minimal damage to healthy cells in the surrounding area. Besides, the synergetic effect of combination of HC with DOX treatment at 0.5 mM and 1 mM concentration can be observed in Figure 18 for all the cells. However, when the concentration is increased to 2 mM, the DOX effect is dominant, and HC contribution becomes insignificant for Beas-2B and A549 cells. Although all cells respond to the HC-enhanced DOX treatment significantly, the level of response of each cell varies, which could be due to cellular metabolism, mechano-transduction ability, and mechanical properties of the cells.

The interaction among intracellular, mechanical, and viscoelastic elements (e.g., filaments, extracellular matrix, and membranous organelles, their unique configuration, and characteristics) and the deformation of each element in response to external physical impact is a complex relationship in the deformation of biological entities [89]. Besides, the mechanical properties of individual cells could influence biological responses to the same stimulus. It is known that the cell stiffness reflects many vital processes in the cell and sheds light on the potential of HC, which can be considered as a relatively new topic in biomedical applications. The assessment of the interaction of HC with cell biomechanics could pave way to a wide variety of applications of this technique. In this study, it is highlighted that HC could exhibit a more effective anticancer activity, especially when used with anticancer drugs, which is associated with the change in stiffness values of cells upon exposure to HC. In more detail, the mean stiffness values of A549 lung cancer cells are higher compared to BEAS-2B lung cells, which can be explained by the fact that these two different cells have different actin filament organizations and cytoskeletal structures. Besides, A549 cells have a morphologically smaller profile and more compact structure, and proliferative closely with neighboring cells. BEAS-2B cells, on the other hand,

constitute a cell line with larger morphology and are well spread compared to A549 cells. Reczynska et al. [90] examined the stiffness values of these two cell lines with AFM and similarly reported that A549 cells were stiffer than BEAS-2B cells. As stated in various sources, cell stiffness is closely associated with actin stress fibers in the cell cytoplasm. It is known that when these fibers depolymerize and decrease, the cell stiffness decreases. On the contrary, the denser and more organized actin filaments make the cell more rigid, and this stiffer membrane makes the cell more prone to damage when interacting with microbubbles, which has also been shown in ultrasonication applications [91]. This suggests that pores are formed on the surface of stiffer cells, similar to ultrasonic cavitation, due to HC, which increases drug penetration.

HC can provide spatial control over the cells, and the desired impact could be achieved by managing the mechanical impact on cells and cavitation location. Ultimately, HC generated by well-designed HCO device offers different regions of cellular response, which facilitates in-depth investigation of biophysical responses by a single device within few minutes. Precise targeting of cells with cavitating flow could allow for the control of the parameters in drug delivery, which results in minor damage for normal cells compared to cancer cells.

4. CONCLUSIONS AND FUTURE RESEARCH DIRECTIONS

A new concept of ‘hydrodynamic cavitation-on-chip’ was proposed here for the detection of CTCs. This method is advantageous since it is label-free and has short on-chip residence times. In the first part of this study, cavitating inception of four different fluids: the RPMI 1640 medium, Jurkat group, CTC, and Jurkats + CTC group were employed. Results demonstrated that earlier inception was obtained in the group with CTCs. The significant difference among inception pressures of experimental groups, especially between with and without CTC, led us to benefit from the cavitation phenomenon for CTC detection. The effects of different concentrations of CTCs were assessed to investigate the HCOC concept further. Moreover, blood tests were performed to compare the effect of different blood samples from healthy volunteers on cavitation inception. Blood samples from different individuals have approximately the same cavitation inception, while CTC-spiked blood results in significantly lower cavitation inception. Nonetheless, the microfluidic device design will be further considered, and the effect of cell properties on the system will be investigated in detail in subsequent studies for more advanced and sensitive detection applications of the HCOC system. The number of CTCs (concentration) will be reduced to a lower limit of the counted CTC number in the metastatic cancer group in literature, and CTC detection utilizing cavitation in this limit will be evaluated. HCOC concept could achieve early CTC detection so that we expect this inexpensive microfluidic approach with a facile operation procedure. The second chapter of the thesis presents comprehensive results related to *in vitro* biological applications of the HCOC concept. Performed *in vitro* experiments demonstrate that micro-scale HC, which is an emerging tool in biological applications, is a promising approach to investigate different cellular responses and to increase the chemotherapeutic efficacy of the anticancer drug DOX. Within the scope of experimental studies, cell proliferation assay reveals a more pronounced anticancer activity on cancer cells treated with the combination of DOX + HC compared to cells treated with DOX alone. HC has a more dominant cytotoxic effect on cancer cells than normal cells. Beas-2B cells have more viability compared to A549 cells. Upon cavitation exposure, an indistinct number of dead cells are found at locations adjacent to the cavitation zone. In addition, with the use of CDs, it is proven that HC has more anticancer activity by increasing the DOX penetration of cancer cells. Optimization of

this approach is required to obtain a deeper understanding of the physical mechanisms causing cell membrane permeabilization. Finally, changes in the cell stiffness, which is associated with cell proliferation, migration, and metastasis, upon treatment with HC, are examined. Different mechanical characteristics of cancer and normal cells lead to dissimilar bio responses in terms of the level of change in permeability, which is linked with cellular uptake.

5. REFERENCES

- [1] J. Ferlay, M. Colombet, I. Soerjomataram, D.M. Parkin, M. Piñeros, A. Znaor, F. Bray, Cancer statistics for the year 2020: An overview., *Int. J. Cancer.* (2021). <https://doi.org/10.1002/ijc.33588>.
- [2] J. Grueneisen, J. Nagarajah, C. Buchbender, O. Hoffmann, B.M. Schaarschmidt, T. Poeppel, M. Forsting, H.H. Quick, L. Umutlu, S. Kinner, Positron emission tomography/magnetic resonance imaging for local tumor staging in patients with primary breast cancer: a comparison with positron emission tomography/computed tomography and magnetic resonance imaging, *Invest. Radiol.* 50 (2015) 505–513.
- [3] S. Vanharanta, J. Massagué, Origins of Metastatic Traits, *Cancer Cell.* 24 (2013). <https://doi.org/10.1016/j.ccr.2013.09.007>.
- [4] E. Racila, D. Euhus, A.J. Weiss, C. Rao, J. McConnell, L.W.M.M. Terstappen, J.W. Uhr, Detection and characterization of carcinoma cells in the blood, *Proc. Natl. Acad. Sci.* 95 (1998) 4589–4594.
- [5] M.M. Ferreira, V.C. Ramani, S.S. Jeffrey, Circulating tumor cell technologies, *Mol. Oncol.* 10 (2016) 374–394.
- [6] S. Sleijfer, J.-W. Gratama, A.M. Sieuwerts, J. Kraan, J.W.M. Martens, J.A. Foekens, Circulating tumour cell detection on its way to routine diagnostic implementation?, *Eur. J. Cancer.* 43 (2007) 2645–2650.
- [7] M. Ilie, V. Hofman, E. Long-Mira, E. Selva, J.-M. Vignaud, B. Padovani, J. Mouroux, C.-H. Marquette, P. Hofman, “Sentinel” circulating tumor cells allow early diagnosis of lung cancer in patients with chronic obstructive pulmonary disease, *PLoS One.* 9 (2014) e111597.
- [8] V. Zieglschmid, C. Hollmann, O. Böcher, Detection of disseminated tumor cells in peripheral blood, *Crit. Rev. Clin. Lab. Sci.* 42 (2005) 155–196.
- [9] M. Poudineh, E.H. Sargent, K. Pantel, S.O. Kelley, Profiling circulating tumour cells and other biomarkers of invasive cancers, *Nat. Biomed. Eng.* 2 (2018) 72–84.
- [10] E. Sollier, D.E. Go, J. Che, D.R. Gossett, S. O’Byrne, W.M. Weaver, N. Kummer, M. Rettig, J. Goldman, N. Nickols, Size-selective collection of circulating tumor cells using Vortex technology, *Lab Chip.* 14 (2014) 63–77.

- [11] J. Weitz, P. Kienle, J. Lacroix, F. Willeke, A. Benner, T. Lehnert, C. Herfarth, M. von Knebel Doeberitz, Dissemination of tumor cells in patients undergoing surgery for colorectal cancer., *Clin. Cancer Res.* 4 (1998) 343–348.
- [12] M. Balic, N. Dandachi, G. Hofmann, H. Samonigg, H. Loibner, A. Obwaller, A. Van Der Kooi, A.G.J. Tibbe, G. V Doyle, L.W.M.M. Terstappen, Comparison of two methods for enumerating circulating tumor cells in carcinoma patients, *Cytom. Part B Clin. Cytom. J. Int. Soc. Anal. Cytol.* 68 (2005) 25–30.
- [13] V. Gupta, I. Jafferji, M. Garza, V.O. Melnikova, D.K. Hasegawa, R. Pethig, D.W. Davis, ApoStream™, a new dielectrophoretic device for antibody independent isolation and recovery of viable cancer cells from blood, *Biomicrofluidics.* 6 (2012) 24133.
- [14] L.F. Ogle, J.G. Orr, C.E. Willoughby, C. Hutton, S. McPherson, R. Plummer, A. V Boddy, N.J. Curtin, D. Jamieson, H.L. Reeves, Imagestream detection and characterisation of circulating tumour cells—A liquid biopsy for hepatocellular carcinoma?, *J. Hepatol.* 65 (2016) 305–313.
- [15] E.P. Rood, *Mechanisms of cavitation inception*, (1991).
- [16] C.E. Brennen, *Cavitation and bubble dynamics*, Cambridge University Press, 2014.
- [17] S.S. Sarraf, F.R. Talabazar, I. Namli, M. Maleki, A.S. Aghdam, G. Gharib, D. Grishenkov, M. Ghorbani, A. Kosar, *Fundamentals, Biomedical Applications and Future Potential of Micro-scale Cavitation-A Review*, *Lab Chip.* (2022).
- [18] C. Mishra, Y. Peles, Cavitation in flow through a micro-orifice inside a silicon microchannel, *Phys. Fluids.* 17 (2005) 013601. <https://doi.org/10.1063/1.1827602>.
- [19] P. Eisenberg, Discussion:“Scale Effects on Cavitation”(Holl, J. William, and Wislicenus, George F., 1961, *ASME J. Basic Eng.*, 83, pp. 385–395), (1961).
- [20] C. Parsons, *The Steam Turbine on Land at Sea*, Smithsonian Inst., 1908.
- [21] M. Shehadul Islam, A. Aryasomayajula, P.R. Selvaganapathy, A Review on Macroscale and Microscale Cell Lysis Methods, *Micromachines.* 8 (2017) 83. <https://doi.org/10.3390/mi8030083>.
- [22] J. Kim, M. Johnson, P. Hill, B.K. Gale, Microfluidic sample preparation: cell lysis and nucleic acid purification, *Integr. Biol.* 1 (2009) 574–586. <https://doi.org/10.1039/b905844c>.

- [23] X. Liu, J. Li, L. Zhang, X. Huang, U. Farooq, N. Pang, W. Zhou, L. Qi, L. Xu, L. Niu, Cell Lysis Based on an Oscillating Microbubble Array, *Micromachines*. 11 (2020) 288.
- [24] P.A. Quinto-Su, H.-H. Lai, H.H. Yoon, C.E. Sims, N.L. Allbritton, V. Venugopalan, Examination of laser microbeam cell lysis in a PDMS microfluidic channel using time-resolved imaging, *Lab Chip*. 8 (2008) 408–414.
- [25] B. Wang, H. Su, B. Zhang, Hydrodynamic cavitation as a promising route for wastewater treatment—A review, *Chem. Eng. J.* 412 (2021) 128685.
- [26] M. Capocellia, M. Prisciandarob, A. Lanciac, D. Musmarraa, Comparison between hydrodynamic and acoustic cavitation in microbial cell disruption, *Chem. Eng.* 38 (2014) 13–18.
- [27] S.S. Save, A.B. Pandit, J.B. Joshi, Use of hydrodynamic cavitation for large scale microbial cell disruption, *Food Bioprod. Process.* 75 (1997) 41–49.
- [28] M.W. Miller, D.L. Miller, A.A. Brayman, A review of in vitro bioeffects of inertial ultrasonic cavitation from a mechanistic perspective, *Ultrasound Med. Biol.* 22 (1996) 1131–1154.
- [29] T. Tandiono, S.-W. Ohl, C.S.-H. Chin, D.S.-W. Ow, C.-D. Ohl, Cell lysis using acoustic cavitation bubbles in microfluidics, *J. Acoust. Soc. Am.* 132 (2012) 1953.
- [30] S.S. Save, A.B. Pandit, J.B. Joshi, Microbial cell disruption: role of cavitation, *Chem. Eng. J. Biochem. Eng. J.* 55 (1994) B67–B72.
- [31] M.T. Gevari, G. Aydemir, G. Gharib, O. Kutlu, H. Uvet, M. Ghorbani, A. Koşar, Local Carpet Bombardment of Immobilized Cancer Cells With Hydrodynamic Cavitation, *IEEE Access*. 9 (2021) 14983–14991.
- [32] A.M. Kaba, H. Jeon, A. Park, K. Yi, S. Baek, A. Park, D. Kim, Cavitation-microstreaming-based lysis and DNA extraction using a laser-machined polycarbonate microfluidic chip, *Sensors Actuators B Chem.* 346 (2021) 130511.
- [33] D.A. Lavan, T. McGuire, R. Langer, Small-scale systems for in vivo drug delivery, *Nat. Biotechnol.* 21 (2003) 1184–1191.
- [34] R. Riahi, A. Tamayol, S.A.M. Shaegh, A.M. Ghaemmaghani, M.R. Dokmeci, A. Khademhosseini, Microfluidics for advanced drug delivery systems, *Curr. Opin. Chem. Eng.* 7 (2015) 101–112.

- [35] A.N. Hellman, K.R. Rau, H.H. Yoon, V. Venugopalan, Biophysical Response to Pulsed Laser Microbeam-Induced Cell Lysis and Molecular Delivery, *J. Biophotonics*. 1 (2008) 24–35.
- [36] L. Meng, X. Liu, Y. Wang, W. Zhang, W. Zhou, F. Cai, F. Li, J. Wu, L. Xu, L. Niu, Sonoporation of cells by a parallel stable cavitation microbubble array, *Adv. Sci.* 6 (2019) 1900557.
- [37] X. Guo, C. Cai, G. Xu, Y. Yang, J. Tu, P. Huang, D. Zhang, Interaction between cavitation microbubble and cell: A simulation of sonoporation using boundary element method (BEM), *Ultrason. Sonochem.* 39 (2017) 863–871.
- [38] S. Le Gac, E. Zwaan, A. van den Berg, C.-D. Ohl, Sonoporation of suspension cells with a single cavitation bubble in a microfluidic confinement, *Lab Chip*. 7 (2007) 1666–1672.
- [39] Z.G. Li, A.Q. Liu, E. Klaseboer, J.B. Zhang, C.D. Ohl, Single cell membrane poration by bubble-induced microjets in a microfluidic chip, *Lab Chip*. 13 (2013) 1144–1150.
- [40] G. Peruzzi, G. Sinibaldi, G. Silvani, G. Ruocco, C.M. Casciola, Perspectives on cavitation enhanced endothelial layer permeability, *Colloids Surfaces B Biointerfaces*. 168 (2018) 83–93.
- [41] K. Ronaldson-Bouchard, G. Vunjak-Novakovic, Organs-on-a-chip: a fast track for engineered human tissues in drug development, *Cell Stem Cell*. 22 (2018) 310–324.
- [42] U. Marx, T. Akabane, T.B. Andersson, E. Baker, M. Beilmann, S. Beken, S. Brendler-Schwaab, M. Cirit, R. David, E.-M. Dehne, Biology-inspired microphysiological systems to advance patient benefit and animal welfare in drug development, *ALTEX*. 37 (2020) 365.
- [43] L. Cucullo, P.-O. Couraud, B. Weksler, I.-A. Romero, M. Hossain, E. Rapp, D. Janigro, Immortalized human brain endothelial cells and flow-based vascular modeling: a marriage of convenience for rational neurovascular studies, *J. Cereb. Blood Flow Metab.* 28 (2008) 312–328.
- [44] L. Cucullo, M.S. McAllister, K. Kight, L. Krizanac-Bengez, M. Marroni, M.R. Mayberg, K.A. Stanness, D. Janigro, A new dynamic in vitro model for the multidimensional study of astrocyte–endothelial cell interactions at the blood–brain barrier, *Brain Res.* 951 (2002) 243–254.

- [45] J.D. Wang, E.-S. Khafagy, K. Khanafer, S. Takayama, M.E.H. ElSayed, Organization of endothelial cells, pericytes, and astrocytes into a 3D microfluidic in vitro model of the blood–brain Barrier, *Mol. Pharm.* 13 (2016) 895–906.
- [46] Z. Wang, C. Tirupathi, J. Cho, R.D. Minshall, A.B. Malik, Delivery of nanoparticle-complexed drugs across the vascular endothelial barrier via caveolae, *IUBMB Life.* 63 (2011) 659–667.
- [47] S. Azzi, J.K. Hebda, J. Gavard, Vascular permeability and drug delivery in cancers, *Front. Oncol.* 3 (2013) 211.
- [48] Y. Qiu, S. Tong, L. Zhang, Y. Sakurai, D.R. Myers, L. Hong, W.A. Lam, G. Bao, Magnetic forces enable controlled drug delivery by disrupting endothelial cell-cell junctions, *Nat. Commun.* 8 (2017) 1–10.
- [49] G. Silvani, C. Scognamiglio, D. Caprini, L. Marino, M. Chinappi, G. Sinibaldi, G. Peruzzi, M.F. Kiani, C.M. Casciola, Reversible Cavitation-Induced Junctional Opening in an Artificial Endothelial Layer, *Small.* 15 (2019) 1905375.
- [50] V.E. Ahmadi, I. Butun, R. Altay, S.R. Bazaz, H. Alijani, S. Celik, M.E. Warkiani, A. Koşar, The effects of baffle configuration and number on inertial mixing in a curved serpentine micromixer: Experimental and numerical study, *Chem. Eng. Res. Des.* 168 (2021) 490–498.
- [51] C.-Y. Lee, L.-M. Fu, Recent advances and applications of micromixers, *Sensors Actuators B Chem.* 259 (2018) 677–702.
- [52] K. Erdem, V.E. Ahmadi, A. Kosar, L. Kuddusi, Differential sorting of microparticles using spiral microchannels with elliptic configurations, *Micromachines.* 11 (2020) 412.
- [53] K. Petkovic, G. Metcalfe, H. Chen, Y. Gao, M. Best, D. Lester, Y. Zhu, Rapid detection of Hendra virus antibodies: an integrated device with nanoparticle assay and chaotic micromixing, *Lab Chip.* 17 (2017) 169–177.
- [54] T.-H. Wu, Y. Chen, S.-Y. Park, J. Hong, T. Teslaa, J.F. Zhong, D. Di Carlo, M.A. Teitell, P.-Y. Chiou, Pulsed laser triggered high speed microfluidic fluorescence activated cell sorter, *Lab Chip.* 12 (2012) 1378–1383.
- [55] Y. Chen, A.J. Chung, T. Wu, M.A. Teitell, D. Di Carlo, P. Chiou, Pulsed laser activated cell sorting with three dimensional sheathless inertial focusing, *Small.* 10 (2014) 1746–1751.
- [56] S. Yan, D. Yuan, Q. Zhao, J. Zhang, W. Li, The continuous concentration of

- particles and cancer cell line using cell margination in a groove-based channel, *Micromachines*. 8 (2017) 315.
- [57] G. Wang, Microfluidic cell separation based on cell stiffness, (2014).
- [58] M.T. Gevari, A.H. Shafaghi, L.G. Villanueva, M. Ghorbani, A. Koşar, Engineered Lateral Roughness Element Implementation and Working Fluid Alteration to Intensify Hydrodynamic Cavitating Flows on a Chip for Energy Harvesting, *Micromachines* 2020, Vol. 11, Page 49. 11 (2019) 49. <https://doi.org/10.3390/MI11010049>.
- [59] M. Ghorbani, G. Deprem, E. Ozdemir, A.R. Motezakker, L.G. Villanueva, A. Kosar, On “Cavitation on Chip” in Microfluidic Devices With Surface and Sidewall Roughness Elements, *J. Microelectromechanical Syst.* 28 (2019) 890–899. <https://doi.org/10.1109/JMEMS.2019.2925541>.
- [60] M. Yu, S. Stott, M. Toner, S. Maheswaran, D.A. Haber, Circulating tumor cells: approaches to isolation and characterization, *J. Cell Biol.* 192 (2011) 373–382.
- [61] L. Xu, J. Shamash, Y.-J. Lu, Circulating Tumor Cells: a window to understand cancer metastasis, monitor and fight against cancers, *J. Can. Res. Updates*. 4 (2015) 13–29.
- [62] S. Meng, D. Tripathy, E.P. Frenkel, S. Shete, E.Z. Naftalis, J.F. Huth, P.D. Beitsch, M. Leitch, S. Hoover, D. Euhus, Circulating tumor cells in patients with breast cancer dormancy, *Clin. Cancer Res.* 10 (2004) 8152–8162.
- [63] I. Nel, E.W. Morawetz, D. Tschodu, J.A. Käs, B. Aktas, The Mechanical Fingerprint of Circulating Tumor Cells (CTCs) in Breast Cancer Patients, *Cancers (Basel)*. 13 (2021) 1119.
- [64] Z. El-Schich, B. Janicke, K. Alm, N. Dizeyi, J. L Persson, A. Gjörlöff Wingren, Discrimination between breast cancer cells and white blood cells by non-invasive measurements: Implications for a novel in vitro-based circulating tumor cell model using digital holographic cytometry, *Appl. Sci.* 10 (2020) 4854.
- [65] N. Touil, R. Hadeif, A. Lemnouer, A. Zrara, A.I. Sbai, B. Belfquih, S. Mrani, A. Benkirane, M. Ouaaline, M. Mrabet, Range-reference determination of lymphocyte subsets in Moroccan blood donors, *Afr. Health Sci.* 12 (2012) 334–338.
- [66] I. Del Giudice, F.R. Mauro, M.S. De Propriis, S. Santangelo, M. Marinelli, N. Peragine, V. Di Maio, M. Nanni, R. Barzotti, F. Mancini, White blood cell count

- at diagnosis and immunoglobulin variable region gene mutations are independent predictors of treatment-free survival in young patients with stage A chronic lymphocytic leukemia, *Haematologica*. 96 (2011) 626.
- [67] W.-S. Tsai, J.-S. Chen, H.-J. Shao, J.-C. Wu, J.-M. Lai, S.-H. Lu, T.-F. Hung, Y.-C. Chiu, J.-F. You, P.-S. Hsieh, Circulating tumor cell count correlates with colorectal neoplasm progression and is a prognostic marker for distant metastasis in non-metastatic patients, *Sci. Rep.* 6 (2016) 1–8.
- [68] M. Giuliano, A. Shaikh, H.C. Lo, G. Arpino, S. De Placido, X.H. Zhang, M. Cristofanilli, R. Schiff, M. V Trivedi, Perspective on circulating tumor cell clusters: why it takes a village to metastasize, *Cancer Res.* 78 (2018) 845–852.
- [69] S.H. Au, J. Edd, A.E. Stoddard, K.H.K. Wong, F. Fachin, S. Maheswaran, D.A. Haber, S.L. Stott, R. Kapur, M. Toner, Microfluidic isolation of circulating tumor cell clusters by size and asymmetry, *Sci. Rep.* 7 (2017) 1–10.
- [70] H. Nielsen, P.H. Petersen, U. Feldt-Rasmussen, V. Binder, Variations in plasma protein concentrations in individuals with ulcerative colitis: analytical and biological factors, *Scand. J. Clin. Lab. Invest.* 39 (1979) 495–502.
- [71] D.S. Micalizzi, S. Maheswaran, D.A. Haber, A conduit to metastasis: circulating tumor cell biology, *Genes Dev.* 31 (2017) 1827–1840.
- [72] M. Hensler, I. Vančurová, E. Becht, O. Palata, P. Strnad, P. Tesařová, M. Čabiňáková, D. Švec, M. Kubista, J. Bartůňková, Gene expression profiling of circulating tumor cells and peripheral blood mononuclear cells from breast cancer patients, *Oncoimmunology*. 5 (2016) e1102827.
- [73] A. Hosseinpour Shafaghi, F. Rokhsar Talabazar, M. Zuvin, M. Talebian Gevari, L.G. Villanueva, M. Ghorbani, A. Koşar, On cavitation inception and cavitating flow patterns in a multi-orifice microfluidic device with a functional surface, *Phys. Fluids*. 33 (2021) 032005. <https://doi.org/10.1063/5.0037736>.
- [74] Y. Hiraoka, K. Kimbara, Rapid assessment of the physiological status of the polychlorinated biphenyl degrader *Comamonas testosteroni* TK102 by flow cytometry, *Appl. Environ. Microbiol.* 68 (2002) 2031–2035.
- [75] R. Varol, S. Omeroglu, Z. Karavelioglu, G. Aydemir, A. Karadag, H.E. Meco, G.C. Kocal, M.E. Oruc, G.B. Esmer, Y. Basbinar, Holographic Cell Stiffness Mapping Using Acoustic Stimulation, *ArXiv Prepr. ArXiv2102.07480*. (2021).
- [76] G. Chakravarty, A. Mathur, P. Mallade, S. Gerlach, J. Willis, A. Datta, S.

- Srivastav, A.B. Abdel-Mageed, D. Mondal, Nelfinavir targets multiple drug resistance mechanisms to increase the efficacy of doxorubicin in MCF-7/Dox breast cancer cells, *Biochimie*. 124 (2016) 53–64.
- [77] X. Tai, X. Cai, Z. Zhang, R. Wei, In vitro and in vivo inhibition of tumor cell viability by combined dihydroartemisinin and doxorubicin treatment, and the underlying mechanism, *Oncol. Lett.* 12 (2016) 3701–3706.
- [78] F. Rokhsar Talabazar, M. Jafarpour, M. Zuvin, H. Chen, M.T. Gevari, L.G. Villanueva, D. Grishenkov, A. Koşar, M. Ghorbani, Design and fabrication of a vigorous “cavitation-on-a-chip” device with a multiple microchannel configuration, *Microsystems Nanoeng.* 7 (2021) 44. <https://doi.org/10.1038/s41378-021-00270-1>.
- [79] B. Balasundaram, S.T.L. Harrison, Disruption of Brewers’ yeast by hydrodynamic cavitation: Process variables and their influence on selective release, *Biotechnol. Bioeng.* 94 (2006) 303–311.
- [80] A.K. Lee, D.M. Lewis, P.J. Ashman, Microalgal cell disruption by hydrodynamic cavitation for the production of biofuels, *J. Appl. Phycol.* 27 (2015) 1881–1889.
- [81] S. Alam, D.B. Lovett, R.B. Dickinson, K.J. Roux, T.P. Lele, Nuclear forces and cell mechanosensing, *Prog. Mol. Biol. Transl. Sci.* 126 (2014) 205–215.
- [82] Z. Jahed, M. Soheilypour, M. Peyro, M.R.K. Mofrad, The LINC and NPC relationship—it’s complicated!, *J. Cell Sci.* 129 (2016) 3219–3229.
- [83] B. Enyedi, P. Niethammer, Nuclear membrane stretch and its role in mechanotransduction, *Nucleus*. 8 (2017) 156–161.
- [84] O.K. Kosheleva, T.-C. Lai, N.G. Chen, M. Hsiao, C.-H. Chen, Selective killing of cancer cells by nanoparticle-assisted ultrasound, *J. Nanobiotechnology*. 14 (2016) 1–11.
- [85] P. Fan, Y. Zhang, X. Guo, C. Cai, M. Wang, D. Yang, Y. Li, J. Tu, L.A. Crum, J. Wu, Cell-cycle-specific cellular responses to sonoporation, *Theranostics*. 7 (2017) 4894.
- [86] D. Needham, H.P. Ting-Beall, R. Tran-Son-Tay, A physical characterization of GAP A3 hybridoma cells: morphology, geometry, and mechanical properties, *Biotechnol. Bioeng.* 38 (1991) 838–852.
- [87] E. Nogales, Structural insights into microtubule function, *Annu. Rev. Biochem.* 69 (2000) 277–302.

- [88] M. Wang, Y. Zhang, C. Cai, J. Tu, X. Guo, D. Zhang, Sonoporation-induced cell membrane permeabilization and cytoskeleton disassembly at varied acoustic and microbubble-cell parameters, *Sci. Rep.* 8 (2018) 1–12.
- [89] Q. Wang, K. Manmi, K.-K. Liu, Cell mechanics in biomedical cavitation, *Interface Focus.* 5 (2015) 20150018.
- [90] K. Reczyńska, D. Khanal, K. Pielichowska, E. Pamuła, W. Chrzanowski, Distinct Influence of Saturated Fatty Acids on Malignant and Nonmalignant Human Lung Epithelial Cells, *Lipids.* 55 (2020) 117–126.
- [91] M.A. Khayamian, M. Baniassadi, M. Abdolahad, Monitoring the effect of sonoporation on the cells using electrochemical approach, *Ultrason. Sonochem.* 41 (2018) 619–625.